ABSTRACT

PHOTOPLETHYSMOGRAPH-DERIVED RESPIRATION

by
Priyanka Pankaj Shah

Stress & Motivated Behavioral Institute (SMBI) has developed a research program to provide an objective evaluation of the physiological and neurocognitive impact of human electromuscular muscular interference (HEMI) devices in humans. The initial step is to understand their physiological impact, which is characterized by vital signs. Volunteers are recruited from HEMI training programs with the provision that data collection can not interfere with training. Thus, an ambulatory system was assembled. There are two main issues in the *current* ambulatory system, one of which is the reliability of the respiration signal obtained using a strain gauge respiration band, mainly due to motion artifact.

The field of monitoring heart rate and respiratory rate using the photoplethysmograph (PPG) signal is rapidly growing. The main objectives of the thesis is to design a PPG hardware – an ear clip sensor and analog processing circuit – to comprise respiration related information and build a software using autoregressive modeling technique to extract respiratory rate from the PPG signal. The custom hardware and software verification results are compared with that of off-the-shelf Nonin® pulse oximetry module – Xpod®. The custom hardware PPG signal was affected more significantly by motion artifact than the Xpod® hardware output. Discrepancies in detecting 6 breaths per minute using custom PPG signal were noted. In conclusion, a few changes in the custom hardware circuit are suggested to further improve the software results in an ambulatory setting. In addition, a more controlled study is suggested.

PHOTOPLETHYSMOGRAPH-DERIVED RESPIRATION

by
Priyanka Pankaj Shah

A Thesis
Submitted to the Faculty of
New Jersey Institute of Technology
in Partial Fulfillment of the Requirements for the Degree of
Master of Science in Biomedical Engineering

Department of Biomedical Engineering

May 2008

APPROVAL PAGE

PHOTOPLETHYSMOGRAPH-DERIVED RESPIRATION

Priyanka Pankaj Shah

Dr. Lisa Simone, Thesis Advisor Assistant Research Professor of Biomedical Engineering, NJIT	Date
Mr. Michael T. Bergen, Committee Member Veterans Affairs New Jersey Health Care Center, East Orange, NJ Adjunct Professor of Biomedical Engineering, NJIT	Date
Dr. Ali Akansu, Committee Member Professor of Electrical and Computer Engineering, NJIT	Date
Dr. Richard Servatius, Committee Member Professor of Neuroscience, UMDNJ	Date
Dr. Joel Schesser, Committee Member University Lecturer of Biomedical Engineering, NJIT	Date
Dr. Richard Foulds, Committee Member Professor of Biomedical Engineering, NJIT	Date

BIOGRAPHICAL SKETCH

Author: Priyanka Pankaj Shah

Degree: Master of Science

Date: May 2008

Undergraduate and Graduate Education:

- Master of Science in Biomedical Engineering,
  New Jersey Institute of Technology, Newark, NJ, 2008

- Bachelor of Science in Biomedical Engineering,
  New Jersey Institute of Technology, Newark, NJ, 2006

Major: Biomedical Engineering

To my Papa, Mummy, Anjumami and Dadaji

ACKNOWLEDGMENT

I would like to express my deepest gratitude to Prof. Michael Bergen for his constant support, encouragement, and insight. I would not have been able to achieve my goals, if it was not for his timely help. I also would like to thank Dr. Lisa Simone for her valuable support, guidance and patience. Her help and encouragement played a very important role in the success of this thesis. Special thanks are given to Dr. Schesser, Dr. Ali Akansu, Dr. Richard Servatius, and Dr. Richard Foulds for actively participating in my committee.

I would like to thank my fellow co-workers and friends at Veterans Affairs Medical Center - Gladstone Reid, Florence Chua, Robert DeMarco, Keith Slaski and Jose Chua - for their support and friendship. Their integrity and dedication to work has inspired me to perform better every day.

Words are not enough to express my gratitude toward all the members of my family. I would like to start by thanking my Mom for being so strong through all these years and for all the prayers. She fought through the struggles of life like a warrior and I am really proud of her. Sweet memories of my childhood will always stay with me no matter where I am. Thank you, Dad for always keeping faith in me and for never giving up. His strength, dedication, positive attitude and encouragement have always motivated me to push forward even during the toughest times. I hope I never let him down.

"When a person desires something, all the universe conspires to help that person realize his dream"

– Paulo Coehlo (The Alchemist)

The entire universe conspired to bring 'Anjumami' – my aunt - in my life so that I can realize my dream, my destiny and the path to happiness. Her selflessness and compassion have completely changed my attitude towards life. I would like to take this

opportunity to thank Atulmama – my uncle - for his constant financial support. I look up to him and respect him for his intelligence, dedication and pragmatism. I'll never forget what he has done for me. I would like to thank my grandmother 'Bhabhi', who has always supported my parents and I, in sickness and in health. I am dedicating this thesis to my grandfather – Mr. Rajnikant Parikh - 'Dadaji' to let him know wherever he is that he is not forgotten. He is still missed and loved. Also, I would like to thank Aditi and Chiti – my cousins - for giving me such great memories of the time we have spent together. I am truly blessed with sisters like them. They taught me the most valuable lessons of life -- about love, care, respect, and responsibility and look up to them as my role models.

I would also like to thank all my other family members– my grandparents - 'Ben' and 'Dadaji', Mixamasi - Masa, , Umeshkaka - Kaki, Yoginmama - Smitamami, Yash, Anu, Kinjal, Gunjan - Stuti, Poonam, and Lalita for all their love, support, concern and blessings throughout the years. I love you all so much.

I would like to thank, Sheela Nagaraj, my best friend for her love, friendship and great memories of college. Last but not the least, I want to thank Premjit Basak 'Rony' – my best friend for last 6 years. His unwavering support, love and care have helped me survive through the toughest times.

TABLE OF CONTENTS

TABLE OF CONTENTS
(Continued)

Chapter **Page**

LIST OF TABLES

LIST OF FIGURES

LIST OF FIGURES
(Continued)

LIST OF FIGURES
(Continued)

CHAPTER 1

INTRODUCTION

1.1 Objective

Human electromuscular interruption devices (HEMI) are increasingly popular with law enforcement agencies, whose largest manufacturers are TASER International ((TI), Scottsdale, AZ). TASERs produce electrical discharge to depolarize muscle, induce tetanus, and eliminate voluntary motor control. There are several controversies in the general population related to TASER use by the law enforcement agencies. On one hand, deaths have occurred to individuals while being exposed to TASER by law enforcement in the field, which would question its safety. On the other hand, most law enforcement agencies require or encourage their officers to experience TASER discharge during training. In these cases - numbering as many as 100,000 discharges - no officer deaths have been reported. To provide an objective evaluation of the physiological and neurocognitive impact of TASING, and to infer the health risk in humans, the Stress & Motivated Behavioral Institute (SMBI) at University of Medicine and Dentistry of New Jersey have developed a research programs in humans.

The initial step of this program is to try to understand the physiological impact (muscle, heart and cardiorespiratory alterations) in trainees during their occupational exposure to TASERs. The *physiological* impact of TASERs can be characterized non-invasively by studying changes in vital signs during and after tasing as compared to the baseline.

HEMI training programs are conducted by local law enforcement agencies throughout the United States, but not New Jersey. TI strongly recommends the trainees to

experience the TASER discharge during the training. The volunteers for the SMBI study are, thus, recruited from HEMI training programs with the provision that the data collection can not interfere with training. The physiological data collection becomes challenging as the volunteers are exposed to TASER sometime *during* the training session. A further condition is that the physiological data must be collected pre-TASING, during the TASING and post-TASING. Consequently, tethering volunteers to equipment for the duration of the session, sometimes for several hours, is not feasible. Thus, a need for an ambulatory system to be capable of monitoring vital signs such as: 3-lead electrocardiogram (for heart rate and heart rate variability measurements), respiration, body temperature, and oxygen saturation and body posture, was presented. While the system has broad applicability to other non-tethered data collection applications, it was explicitly assembled to be used for the HEMI study.

The system uses the wireless technology Bluetooth® for data transmission to a central collection station. Custom analog processing units were built in the VA engineering laboratory to apply proper amplification, filtering, and other signal processing tools to the ECG, respiration and body temperature signals. These circuits were designed explicitly to fulfill the input voltage requirements (0 – 5 V; no negative voltages) of the Bluetooth® module used for this study. While the system is performing well for the current experiments, there are a few issues with the ambulatory setup, parts of which are tackled in this thesis.

With the current ambulatory setup, the ECG, respiration, body posture and body temperature custom processing circuit provides an analog output. These signals are then digitized and transmitted wirelessly to the receiver station using BlueSentry™

Bluetooth® module (Roving Networks, California USA) as seen in Figure 1.1. The oxygen saturation measurements are done using off-the-shelf Xpod® evaluation kit pulse oximetry module (Nonin, Inc.). Xpod® is a patented device providing four parameter output: heart rate, oxygen saturation, pulse height, and photoplethysmography at 75 Hz. It produces output in a serial format, which did not match the BlueSentry™ Bluetooth® module analog to digital (ADC) channel input requirement. Thus, a separate Bluetooth® module – BluePort™ (Roving Networks, California USA) was purchased to comply with the Xpod® features. Consequently, an ambulatory pack used for data collection consists of: 1) Custom analog circuits for ECG, body temperature, body posture and respiration, 2) BlueSentry™ module for data transmission, 3) Xpod® for oxygen saturation, heart rate and photoplethysmography measurements and 4) BluePort™ module with a serial input for Xpod® data transmission.

Thus, each ambulatory pack contains two Bluetooth® transmitters. A block diagram of the current system is as shown in Figure 1.1. There are several issues with the current ambulatory setup.

The first issue is the reliability of the respiration signal. The respiration signal, currently, is obtained using a strain gauge band on the chest, which measures the volume changes of the thoracic cavity with inspiration and expiration processes. Essentially, the sensor detects the movement of the thoracic cavity with respiration. This method is prone to motion artifacts. Motion artifacts are apparent prior to exposure and after exposure inasmuch as subjects perform normal activities (e.g., walk, talk, laugh etc). However, the largest source of artifact is during exposure. Subjects are held by spotters and are laid to ground as they lose muscular control. The frequency rate of the artifacts masks

respiration. Thus, from the first stage of data processing, it was clear that the respiratory rate obtained using strain gauge was unreliable.

Bluetooth® technology along with its many attractive features has certain limitations. The Bluetooth® receiver connected to a computer allows connection with only eight Bluetooth® transmitters at once. Thus, with the current ambulatory system setup, only four subjects (ambulatory packs) can be connected to the receiver end on the computer (as seen in Figure 1.1) or eight subjects with two computers. If the number of Bluetooth® transmitters per ambulatory pack is reduced to one then its capability can be increased to have sixteen subjects with two computers at once. This is the second issue with the current ambulatory system.

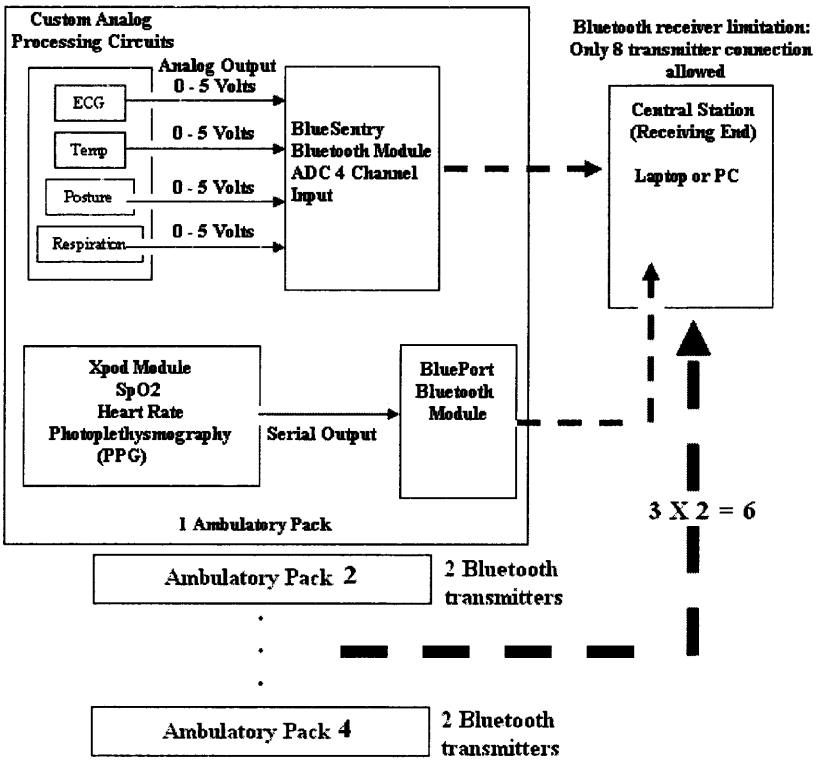

Figure 1.1 Block diagram of current ambulatory system transmitter packs.

Considering all these factors, this thesis is a first step towards incorporating pulse oximetry module with the other parameters on a single Bluetooth® transmitter and to develop a more reliable respiratory rate monitoring unit.

The field of monitoring heart rate and respiratory rate using the photoplethysmograph (PPG) signal is rapidly growing because of its many attractive features including the possibility of undisturbed and long-term monitoring in a non-invasive fashion (Johansson A. et al., 1999). PPG signal is one of the outputs of many pulse oximetry modules. In fact, the oxygen saturation measurement is performed using the PPG signal. The concepts of extracting heart rate and oxygen saturation parameters from the PPG signal are well established (Nilsson et al., 2003). Thus, the main objectives set forth for this thesis are as follows:

- Design software based processing algorithm in LabVIEW to extract respiratory rate from the digitized PPG signal.
- Design a custom PPG module, which includes a sensor and an analog processing unit,
    - To make it compatible to the BlueSentry™ Bluetooth® module input requirements
        - To reduce number Bluetooth® transmitters per pack
        - Reduce cost
    - To match reliability and robustness of Xpod® module
    - To enable a control over the sampling rate, filtering characteristics and quantization/resolution levels of the PPG signal
- To compare the results of the LabVIEW based respiratory rate extraction algorithm using the PPG obtained from the Xpod® and the custom hardware at a known respiratory rate

Accomplishment of these objectives will ultimately serve the final goal, which is to encompass the entire ambulatory system on one Bluetooth® transmitter per ambulatory pack/subject to enhance data collection from eight subjects per computer

instead of 4. This thesis focuses mainly on obtaining respiratory rate from the PPG signal, as concepts of extracting heart rate and oxygen saturation are well established and can be incorporated in the system at a later stage. The future development includes obtaining heart rate and percentage oxygen saturation, along with respiratory rate from a single PPG sensor to make the system even more compact.

A PPG custom hardware circuit and software for respiratory rate extraction were designed in the VA engineering laboratory. Data during several activities and paced breathing (Chapter 3) was collected for a purpose of proof of concept at NJIT from N=1 subject.

1.2 Background Information

1.2.1 Photoplethysmograph

Photoplethysmography (PPG) is a method of applying a light source and a light sensor on the opposite or on the same side of peripheral body parts such as finger, ear lobe, or toe, for measuring the alterations in light intensity that passes through the tissue. The alterations in light intensity are mainly due to the change in the volume in the absorbing materials and due to the scattering effects of light. It is a low cost, simple, portable, and non-invasive technology, usually used for measuring percent oxygen saturation, blood pressure, and cardiac output, and to understand autonomic nervous system function, and peripheral vascular disease in clinical settings. If the light source and the sensor are both placed on the same side of the body part, then the type of probe is called a reflectance probe, while if they are placed on opposite sides then it is called a transmittance probe.

Reflectance probe measures the intensity of light reflected by the tissue sample, while transmittance probe measures the attenuation of incident light intensity after its passage through the sample. According to Anderson and Parrish (1981) (as cited in Webster, 1997), the interaction of light with tissue sample is explained by several optical processes such as scattering, absorption, reflection, transmission and florescence (Webster, 1997).

The attenuation of light is mainly caused by changes in blood volume and in the orientation of blood vessels, and blood vessel wall movement. Thus, a typical PPG signal is related to the circulation of blood through the body parts under study. This signal comprises of two main components: AC and DC. AC is the pulsatile component as detected by the light sensor, pertaining to the synchronous changes in the blood volume with each heart beat. DC component, on the other hand, is related to the slowly changing baseline depending on respiration, sympathetic nervous system activity and thermoregulation (Webster, 1997).

This thesis is mainly concerned with the design of a circuit and a sensor to obtain the PPG signal, and to understand its operation so that highly efficient software based algorithm can be designed to derive the respiratory rate. To understand this procedure more accurately, however, it is essential to comprehend the underlying physiological systems participating in triggering changes in the volume of the peripheral body parts (under study) depending on the blood flow. The circulatory system mainly involving the heart, the blood vessels and the blood is discussed in more detail in the latter sections, to better understand blood flow. Not only that, in order to link the two processes together i.e., PPG and respiratory rate, it is essential to discuss the respiratory system, which is mainly involved in oxygenation of blood through the process of gas exchange in the

lungs. The respiratory system mainly consists of the airways, the lungs, the respiratory muscles.

1.2.2 The Respiratory System

Oxygen plays a vital role in functioning of all the physiological systems in the human body. It manages the process of energy metabolism in the body. Lack of oxygen will cause many processes in the body to work adversely and may cause them irreversible damages. Thus, a prolonged absence of oxygen affects the cells in the body to die.

1.2.2.1 Oxygen Delivery. Ventilation is the first step where the air moves in and out of lungs and gas exchange takes place. Oxygen diffuses into the blood, while carbon dioxide produced during cellular respiration diffuses into the lungs for removal. The oxygenated blood circulates in the entire body until it reaches oxygen-depleted areas. The oxygen is then diffused into the cells and the blood carries the residue gas (carbon dioxide) back to the lungs (Webster, 1997).

Ventilation is defined as the involuntary and rhythmic process of moving air in and out of the lungs. This process is controlled by respiratory neurons in the brain stem, whose output is modulated by chemo-receptors and mechanoreceptors. The respiratory neurons modulate the rate and depth of ventilation. These neurons excite motor neurons in the spinal cord, which in turn causes the contraction of diaphragm, pectoral muscles, and intercostal muscles (respiratory muscles).

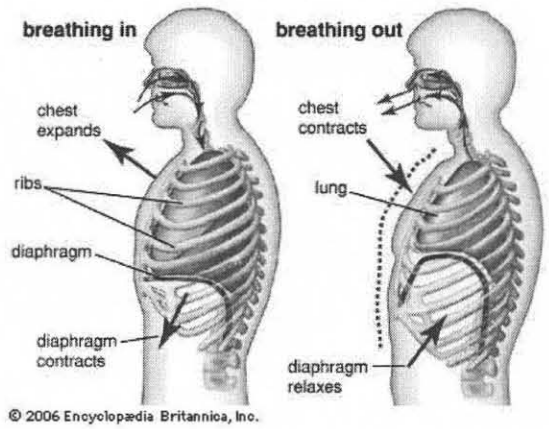

Figure 1.2 Inspiration and expiration (Britannica).

The combined contraction of these muscles pulls the ribcage up and out to give some room for lung expansion – causing inspiration. There is a cyclic inhibition of the activity of respiratory neurons allowing the muscles to relax. This causes the ribcage to contract, which triggers expiration.

1.2.2.2 Oxygen Transport in Blood. Gases are not soluble in blood. The compound hemoglobin provides a secondary method of oxygen transport in a human body. Oxygen transport is also carried out by the oxygen dissolved in plasma. Thus, the total oxygen content in blood is the sum of hemoglobin bound oxygen and the dissolved oxygen.

Hemoglobin is the iron-containing oxygen transport metalloprotein in the red blood cells. It is composed of heme units, which contain molecules of iron, and globin units, which are polypeptide chains. In essence, each subunit of hemoglobin is a globular protein with an embedded heme group; each heme group contains an iron atom, and this is responsible for the binding of oxygen through ion-induced dipole forces. One hemoglobin molecule contains four heme and four globin units. Each heme and globin unit can carry one molecule of oxygen and thus one molecule of hemoglobin can carry

four molecules of oxygen (Weber, 2001). The theory of the working of pulse oximetry lies in the fact that the red blood cells change color depending on the binding state of hemoglobin. An oxygenated molecule is bright red, while deoxygenated is dark red.

The affinity for the oxygen molecules increases as the neutral i.e., completely deoxygenated hemoglobin molecule combines with its first oxygen molecule; this converts a neutral hemoglobin molecule to a negatively charged ion. The affinity further increases with additional combinations. The reverse process is also true. Thus, more molecules bind as the oxygen partial pressure increases until the maximum number is reached. As this limit is approached, only a few additional bindings occur and the curve levels out as the hemoglobin becomes saturated.

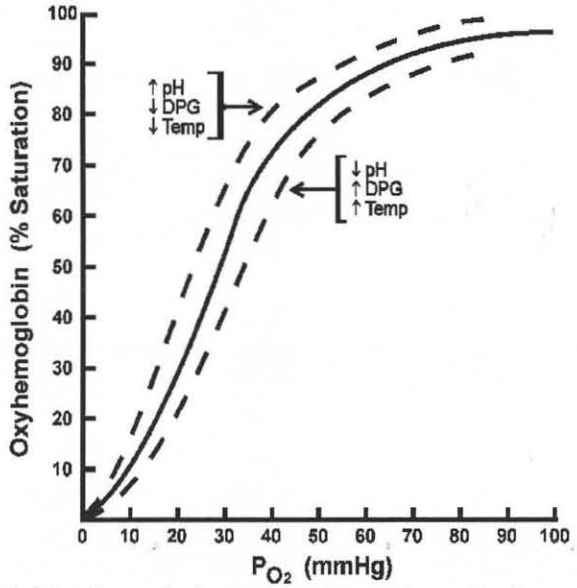

Figure 1.3 Oxyhemoglobin dissociation curve (American Society of Health-System Pharmacists, Inc.).

The curve that shows the relationship between the partial pressure of oxygen in blood and the percentage of oxygen bound to hemoglobin as compared to the maximum

is called oxyhemoglobin dissociation curve. This relationship, as described above, is certainly not linear, but sigmoidal (Webster, 1997).

1.2.3 The Circulatory System

The diffusion of oxygen to the blood occurs by the process of gas exchange in the alveoli of lungs where hemoglobin and plasma act as carriers of oxygen. The oxygenated blood is then returned to the heart for circulation to the rest of the body. The circulatory system is thus involved in transporting oxygenated blood to the cells in the body, where heart is the primary pumping mechanism. It mainly consists of the heart, the blood and the blood vessels. The circulatory system includes: the pulmonary circulation and the systemic circulation (Stern et al., 2001).

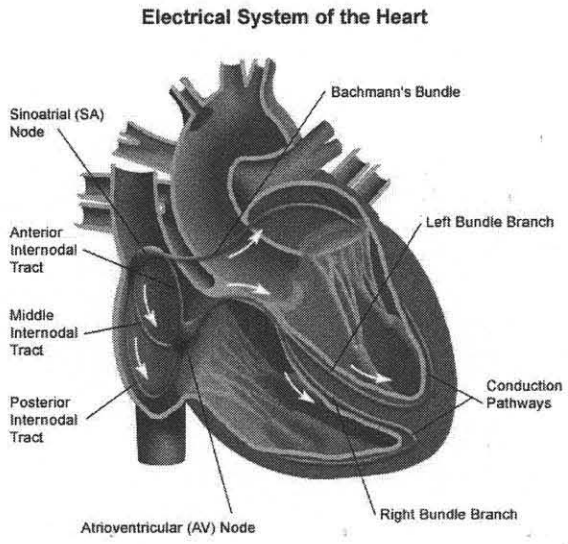

Figure 1.4 The heart (UAB Health System).

The heart has four chambers: right and left atria and right and left ventricles. The right atrium of the heart collects the deoxygenated blood from the body through vena cava and pumps it via the right ventricles in the lungs. As discussed in earlier sections, the process of gas exchange and oxygen delivery takes place in the lungs and the blood is

returned to the left atrium via pulmonary ventral capillaries to larger venules and eventually pulmonary veins. This process is characterized as pulmonary circulation. From the left atrium, the blood travels to the left ventricle and is pumped to the rest of the body via systemic arteries. This is called the systemic circulation.

Blood pressure throughout the arteries varies depending on the activity of the ventricles per heartbeat. It reaches its maximum at the systole, caused by the contraction of the ventricles and at its minimum at the diastole, caused by the ventricular relaxation. This is the basic theory behind the plethysmograph waveform. Plethysmograph is a non-invasive measure of the pulsatile flow of blood in the arteries. The systemic arteries branch into smaller arterioles and even smaller capillaries. Oxygen is then transferred to the tissue in the oxygen-depleted regions. The deoxygenated blood then travels via vein capillaries, venules to the superior vena cava and the inferior vena cava into the right atrium of the heart and the process repeats.

The flow of blood inside the heart is controlled by rhythmic contraction and relaxation of atria and ventricles in an ordered fashion. The electrocardiogram is the measurement of the electrical activity in a single heartbeat modulating the activity of the heart chambers. The rhythmic contraction of the heart is controlled by a series of electrical impulse originating in the sinoatrial (SA) node (60-100 times per minute under normal conditions), the physiological pacemaker. (Stern et al., 2001).

1.2.4 Blood Flow

The brainstem processes several stimuli from the chemoreceptors and baroreceptors to provide a feedback to the SA for controlling the heart rate (i.e., the number times SA

node fires in unit time) and the stroke volume respectively. This process is similar to the respiratory feedback mechanism. The stroke volume is the amount of blood *pumped* by the right and left ventricles in one contraction. The cardiac output is the product of the stroke volume and the heart rate (Stern et al., 2001).

Vasoconstriction is defined as narrowing of the lumen of blood vessels restricting the flow of blood, which cause an increase in blood pressure. The opening of blood vessels is defined as vasodilation. Total peripheral resistance is the cumulative resistance of all the vessels in the systemic circulation (Stern et al. 2001). At each contraction of the heart, blood is forced through the peripheral blood vessels producing dilation or constriction of the vessels. The vasomotor activity is controlled by the autonomic nervous system (ANS). The sympathetic activity makes an important contribution to the redistribution of blood flow when the body's needs change. The parasympathetic nervous system (PNS) generally has a relatively minor effect on the blood vessels. Vasodilation and vasoconstriction change the resistance to blood flow through the vessels. This change in the resistance directly affects both blood flow and blood pressure (Stern et al., 2001) An increase in PPG amplitude indicates sympathetic inhibition (vasodilation) and parasympathetic activation. This implies a greater blood flow to the peripheral vessels. The PPG can display these changes in sympathetic and parasympathetic activities. The physics of photoplethysmography is discussed in more detail in Section 1.2.6.

1.2.5 Link between PPG and Respiration

Many advanced signal processing tools such as digital filtering, Time-Frequency analysis such as Short Time Fourier Transform (STFT) and Wavelets, Time Series analysis using

both parametric and non-parametric modeling techniques, have been applied to establish PPG as a reliable measurement of respiratory rate along with heart rate and oxygen saturation (Nakajima et al., 1995; Addison et al., 2004; Leonard P. A. et al., 2006; Nilsson et al., 2006). Over the years monitoring of heart rate and arterial oxygen saturation and their physiological conditions are well established, while the physiological background for the respiratory rate component of the PPG signal is not fully understood (Nilsson et al., 2003).

Many authors have described the low frequency (LF) variations in the PPG signal as the respiratory-induced intensity variations (RIIV). The PPG signal is also believed to encompass very low frequency (VLF) variations due to the Traube, Hering and Mayer waves in the blood pressure (THM waves) (Penaz, 1978; Traube, 1865; Hering, 1869; Mayer 1876). THM waves are associated with the baroflex loop and thermoregulation, mediated by the sympathetic nervous system (Nilsson et al., 2003). According to Ahmed et al. (1982), THM waves, even though, have a slower frequency than normal respiration frequency, sometimes combine with the low respiratory frequency (as cited in Nilsson et al., 2003).

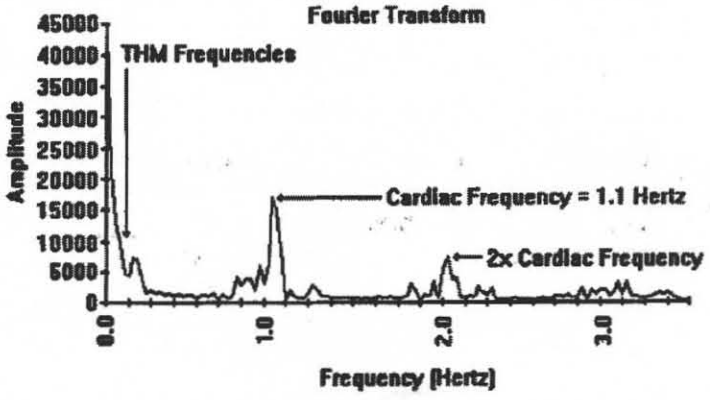

Figure 1.5 Fourier transform of raw PPG signal showing the VLF, LF and high frequency components corresponding to THM waves, RIIV signal and cardiac frequency respectively (Rusch, T. L. et al., 1996).

This thesis is, however mainly concerned with the RIIV signal. RIIV occur because of the changes in the intrathoracic pressure with inspiration and expiration affecting the peripheral venous return to heart, per respiration cycle (Ugnell, 1995; Nilsson et al., 2003; Brecher et al., 1954; Johansson et al., 2000). Brecher G. and Hubay C. (1954) have described a series of alterations taking place in the heart (superior vena cava) and lungs (pulmonary artery) with respiration. These alterations are ultimately transmitted to the periphery and can be detected by the PPG sensors (Nilsson et al., 2003).

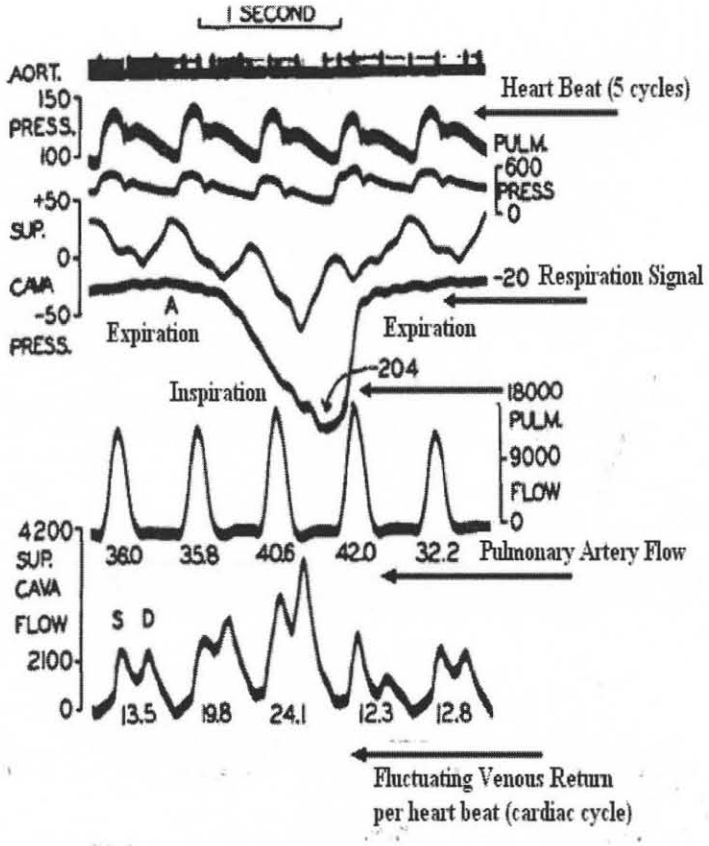

Figure 1.6 Demonstrating fluctuating venous return with each heart beat (Brecher et al., 1954).

Brecher et al. (1955) carried out an invasive experiment on dogs to measure a relationship among several parameters such as the heart beat, stroke volume, venous

return, respiration, and blood pressure. They used flow meters in various designated areas in the body to derive an accurate relationship. The superior caval flow was taken as a representative of venous return and the main pulmonary artery as the right heart output into lungs. Figure 1.5 shows a segment to demonstrate the effect of spontaneous respiration on venous return and cardiac output. The Figure 1.5 shows that pulmonary artery flow increases significantly during spontaneous inspiration (from 36.0 ml during expiration to 42 ml during inspiration and back to 32.2 ml), and that changes in venous return (13.5 ml during expiration to 24.1 ml during inspiration and back to 12.8 ml) are always reflected in the beat output of the following cycle. The greatest venous return increase (24.1 ml.) took place during the third beat when inspiration had reached its maximum. With the onset of expiration the return flow of blood was immediately reduced (fourth heart beat, 12.3 ml.). From this sequence of events, the team concluded that the inspiratory augmentation of venous return was responsible for the increase in the pulmonary artery flow (Brecher et al., 1955). However, the lungs and right ventricle buffer respiratory changes in the systemic venous return, and only minor changes are transmitted to the left ventricle. According to Santanire and Amoore (1994), this phenomenon results in a constant ejected volume (stroke volume) from the left ventricle (as cited in Nilsson et al. 2003). The arterial compliance is more than ten times lower than the venous compliance (Slutter et al., 1981) and make fluctuations in the volume of blood less pronounced on the arterial side of the circulation (Nilsson et al., 2003). Thus, venous variation in blood volume can be considered as a main contributor to the RIIV signal. To prove this relationship, Nilsson et al. (2003) carried out a study to understand the relationship between RIIV and peripheral venous pressure (PVP). They concluded

that there is, in fact, a correlation in the amplitudes of the RIIV in the PPG signal and the respiratory variations in the PVP with varying respiratory pattern.

Fleming et al. (2007) compared several digital filtering, wavelet decomposition and autoregressive (AR) modeling methods currently used to extract respiratory rate from the PPG signal. They concluded that autoregressive modeling method outperformed the other methods and that this method could also be used for real-time tracking of breathing rate using the PPG waveform (Fleming et al., 2007). Based on the results provided by this study, autoregressive modeling method was used to extract respiratory rate information from PPG in this thesis. This method and its application are discussed in detail in Chapter 2.

1.2.6 Light Absorbance in Photoplethysmograph

Photoplethysmograph is a representation of changes in the absorption of light by chromophores in the tissue by detecting changes in light transmission through the vascular bed. The changes in absorption are caused because of changes in blood volume in the blood vessels, especially arteries and arterioles, with each heart beat i.e., ventricular contraction. An absorption spectrum of an absorbing material is unique to the absorbing atoms or molecules that form the material, and such spectrum provides a key for recognizing specific compounds. This is accomplished by applying the Beer-Lambert's law.

1.2.6.1 Beer-Lambert's Law. Beer-Lambert's law quantifies the attenuation of light traveling through a uniform medium containing an absorbing material.

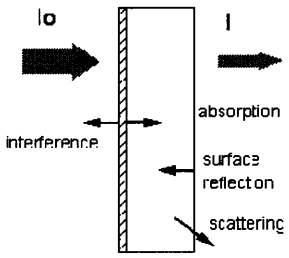

Figure 1.7 Beer Lambert's law.

If a monochromatic light of intensity Io enters a medium, part of this light is transmitted through the medium and the rest is absorbed. Beer's law does not take into account the reflection of the light at the surface and scattering of light in the medium. The law suggests that there is a linear relationship between the absorbance and concentration of the absorbing material, which is represented using the units of molarity. Thus,

$$A = \varepsilon(\lambda) \times c \times b \tag{1.1}$$

$\varepsilon(\lambda)$ = extinction coefficient or absorptivity of the absorbing material at a specific wavelength - λ (L mmol^{-1} cm^{-1})

c = concentration of the absorbing material, which is considered to be a constant (mmol L^{-1}), and

b = optical path length (cm) (distance travelled by the light through the medium)

The Beer-Lambert's law assumes that the medium is homogenous or uniform, the incident light is collimated and reflection and scattering do not contribute to the loss of incident light. By quantized modeling of passage of light through an absorbing but non-scattering medium can be used to obtain Beer-Lambert's law.

The concepts of Beer-Lambert's law can be generalized for the case when more than one material absorbs the incident light in the same medium i.e., the total absorbance is a sum of individual absorbing processes for each material at the same wavelength of

light. The resulting total absorbance of light A_t in a medium consisting of n absorbing materials is the sum of their n independent absorbencies (Webster 1997):

$$A_t = \varepsilon_1(\lambda) \times c_1 \times b_1 + \varepsilon_2(\lambda) \times c_2 \times b_2 + \ldots + \varepsilon_n(\lambda) \times c_n \times b_n = \sum_{i=1}^{n} \varepsilon_i(\lambda) \times c_i \times b_i \tag{1.2}$$

where $\varepsilon_1(\lambda)$ and c_i represent the extinction coefficient and concentration of the absorbing material i and b_i represents the optical path length through each material i.e., this value differs from material to material in the same medium.

In experimental terms, the transmittance (T) of light measured by a light sensor on the other end of the medium is defined as the ratio of transmitted light (I) to the incident light (I_o) (Webster, 1997):

$$T = \frac{I}{Io} = 10^{-\varepsilon * b * c} \tag{1.3}$$

1.2.6.2 Hemoglobin. Hemoglobin is the main absorber of light in human blood at the wavelengths used in PPG. As mentioned in Section 1.2.2.3, the absorbing characteristics of hemoglobin vary with its chemical binding properties and the wavelength of the incident light (based on Beer-Lambert's law). Oxygenated and reduced oxygenated hemoglobin absorb most of the light passing through blood, however presence of other variants of hemoglobin such as methemoglobin, carboxyhemoglobin, sulfhemoglobin, and carboxysulfhemoglobin can alter its color and thus its absorption characteristics.

When hemoglobin is fully saturated i.e., carrying four oxygen molecules, it is called oxygenated. When it is not fully saturated it is called reduced. The hemoglobins (oxygenated and reduced) that are able to bind reversibly with oxygen molecules are called functional.

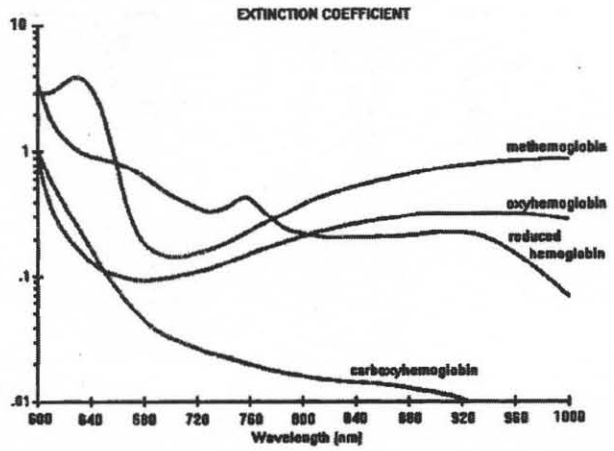

Figure 1.8 Absorbance characteristics of variants of hemoglobin (Heekeren, 1998).

The hemoglobin variants that do not support the transport of oxygen to the tissues, are referred to as dysfunctional hemoglobins. Most of the hemoglobins in human blood are functional. In pulse oximetry and photoplethysmography, the changes due to dysfunctional hemoglobins are ignored (Webster, 1997).

1.2.6.3 Selection of Wavelength of Incident Light for Photoplethysmography. Different species of hemoglobin have different physical properties because of the variations in their chemical structure. Thus, the extinction coefficients of each of the functional and dysfunctional hemoglobin are different at different wavelengths of light. For example, the absorbance of red light by reduced hemoglobin is much higher than oxyhemoglobin, whereas the absorbance of infrared light by reduced hemoglobin is much lower than oxyhemoglobin. The extinction coefficients of both hemoglobins are the same at 805 nm wavelength of incident light, which is called an isosbestic point as seen in Figure 1.8.

Red and infrared region of the electromagnetic spectrum has been used in pulse oximetry and photoplethysmography for several reasons. The wavelength of incident light is selected to reflect changes in absorbance of functional hemoglobin with optimum

efficiency. The main constituent of tissue that forms the skin surface is water. Water absorbs light with ultraviolet and long infrared wavelengths very strongly. The red skin pigmentation (melanin) absorbs a large amount of red light with shorter wavelengths (lower than 600 nm), which takes the emphasis off of oxyhemoglobin and reduced oxyhemoglobin absorbance in the tissue. Therefore, it is not desirable to measure light absorbance in that region. In the absorption spectra of water, there is a region that allows red and near infrared light to pass more easily i.e., less absorbance. This facilitates the measurement of blood flow at these wavelengths.

Large differences in extinction coefficients of reduced and oxy-hemoglobin are desirable so that even a slight change in their arterial concentration will exhibit dramatic changes in their absorbance quantity (Beer-Lambert's law). This enables improved light sensing performance as the changes in the transmitted light are intensified. At 660 nm, the difference in extinction coefficients for the reduced and oxy-hemoglobin is large enough, thus it is a desirable wavelength. The flatness of the absorption spectra at chosen wavelengths is one of the other issues that needs consideration.

A shift in the peak wavelength of the light source will result in a corresponding shift in the extinction coefficient value, which in turn changes the transmitted light intensity. This phenomenon induces large errors in the amplitude of PPG signals. The absorbance spectra of reduced and oxy-hemoglobin are relatively flat at 660 nm and 940 nm (Moyle, 1994; Webster, 1997). Thus, 660 nm and 940 nm are the desirable wavelengths for the incident light for pulse oximetry applications. For photoplethsmography, 940 nm is more desirable because at this wavelength there is a flatter response in absorption spectrum than at 660 nm. So the hardware to compensate

for the alterations in the peak wavelength produced by the light source is not required (Webster, 1997).

The different species of hemoglobin are the main absorbers in arterial and venous blood. Most of the hemoglobin in human blood is either reduced or oxy-hemoglobin. According to Beer-Lambert's law, the total absorbance A_t of a solution containing only reduced and oxy-hemoglobin as absorbing substances is as follows:

$$A_t = \varepsilon_{HbO_2}(\lambda) \times c_{HbO_2} \times b_{HbO_2} + \varepsilon_{Hb}(\lambda) \times c_{Hb} \times b_{Hb} \tag{1.4}$$

This equation holds that assumption that the optical path length b is the same for both species of hemoglobin ($b_{HbO2} = b_{Hb}$). c_{HbO2} and c_{Hb} represent the concentrations ε_{HbO2} and ε_{Hb} represent the extinction coefficients of reduced and oxy-hemoglobin respectively. Values for ε_{HbO2} and ε_{Hb} at 940 nm have been measured by Zijlstra et al (1991) (as cited in Webster, 1997):

Table 1.1 Extinction Coefficients of Oxy and Deoxyhemoglobin at 940 nm

Wavelength (nm)	ε_{Hb}	ε_{HbO2}
940	0.18	0.29

1.2.6.4 Measurement of Pulsation of Blood. In PPG model, the primary light absorbers in *arteries* - the reduced and oxy-hemoglobin are considered to be the only absorbers of importance. A PPG sensor is designed such that light of a particular wavelength (Infrared 940 nanometers – nm) is passed through peripheral body sites such as finger, ear lobe, or toe. A photo detector (light sensor) is placed on the opposite side to the light source with a finger or ear lobe (biological tissue) in the middle. Thus, the level of changes detected reflects the change in absorption of light due to the tissue. The sensor

is designed so that it compensates for the parameters affecting the detection of light other then the absorption process by the tissue.

Light traveling through the tissue is absorbed by various absorbing substances such as skin pigmentation, bones and the arterial and venous blood. According to Beer-Lambert's law, the amount of absorbed (and transmitted) light, in this case, is a function of extinction coefficients and concentrations of the primary absorbers, and the length of the optical path.

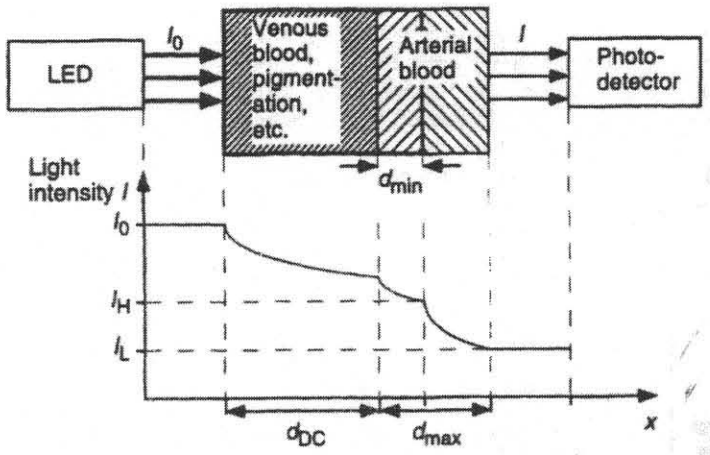

Figure 1.9 Optical path through the tissue bed (Webster, 1997).

The changes in the absorbance quantity occur due to vasoconstriction and vasodilation processes as explained in former sections. The arteries contain more blood during systole than during diastole as the ventricles contract to pressure blood into the rest of the body through the aorta. Vasodilation (increase in diameter) occurs due to the increased pressure in arteries to occupy extra blood from the ventricles before it can reach to the arterioles. This process occurs only in the arteries and arterioles because by the time blood reaches the rest of the peripheral blood vessels (capillaries and veins), the ventricles relax (diastole) and there is a decrease in the pressure exhibited by blood. The

absorbance of light in the tissues with arteries increases as the arteries dilate (greater optical path length b) to occupy extra blood with larger amount of absorbing substances - hemoglobin. During diastole, however the arteries return to their normal state with lesser amount of absorbing substances as b decreases. The photo detector continuously measures the amount of transmitted light to show the total absorbance; 1) the absorbance due to venous blood, constant amount of arterial blood and other non-pulsatile components such as skin pigmentation (non-changing dc component), and 2) the absorbance due to the pulsatile component of the arterial blood (ac component). The pulsatile component of the total absorbance is directly proportional to the amount of absorbing substances present in the blood at that time. Thus, the PPG signal shows the amount of transmitted light detected by the photo detector in a living tissue as a function of time.

The only absorbers present during diastole are the DC components. All the DC components except the non-pulsatile arterial blood are collectively expressed by $\varepsilon_{DC}(\lambda), c_{DC}, b_{DC}$ to equate the intensity of transmitted light. At diastole, the diameter of arterial vessels is at its minimum (b_{min}) and therefore the absorbance of light due to arterial hemoglobin is minimal and the amount of transmitted light is high (I_H).

$$I_H = I_O \times e^{-\varepsilon_{DC}(\lambda)\times c_{DC}\times b_{DC}} \times e^{-(\varepsilon_{HbO_2}(\lambda)\times c_{HbO_2} + \varepsilon_{Hb}(\lambda)\times c_{Hb})b_{\min}} \tag{1.5}$$

While the amount of absorbed light reaches to its maximum during systole and therefore the transmitted light reaches the low peak (I_L). The optical path length in the arteries increases during systole to b_{max}.

$$I_L = I_O \times e^{-\varepsilon_{DC}(\lambda)\times c_{DC}\times b_{DC}} \times e^{-(\varepsilon_{HbO_2}(\lambda)\times c_{HbO_2} + \varepsilon_{Hb}(\lambda)\times c_{Hb})b_{\max}} \tag{1.6}$$

From above equations it can be generalized that the transmitted light intensity I at the photo detector is a function of diameter b of the arteries and arterioles. The diameter changes from bmin to bmax during one cardiac cycle. Thus,

$$\Delta b = b_{\max} - b_{\min} \Rightarrow b_{\max} = \Delta b + b_{\min} \tag{1.7}$$

represents the part of the diameter that changes from 0 to $b_{\max} + b_{\min}$ with time.

By substituting b with $\Delta b + b_{\min}$, I can be expressed as a function of I_H and Δb (Webster, 1997, p. 48):

$$I_L = I_H \times e^{-(\varepsilon_{HbO_2}(\lambda)\times c_{HbO_2} + \varepsilon_{Hb}(\lambda)\times c_{Hb})\Delta b} \tag{1.8}$$

1.2.6.5 Light Scattering. Incident light passing through the tissue is not divided into just absorbed light and transmitted light. Reflection and scattering of incident light takes place, which changes the conclusions derived from Beer-Lambert's law. Unlike the assumptions made under Beer-Lambert's law, blood is not homogeneous and the light source does not produce monochromatic light. The absorbance of light is not simply proportional to the concentration of hemoglobin or to the length of optical path. According to Moyle, if change in the diameter was the only reason, the variation would be much less. The main reasons for increased absorbance are scattering and multiple scattering i.e., sub-scattering. Light scattering occurs when a beam of light is deviated from its initial direction due to a change in index of refraction at the interface of the medium. Thus, discontinuity in the index of refraction at the interface of plasma and of red blood cells produce scattering. According to Steinke and Shepherd (1986), light that is scattered once is likely be scattered again by cells and therefore multiple scattering occurs, which ultimately increases the optical path length (as cited in Webster, 1997).

Therefore, the absorbance increases as the optical path length is increased due to multiple scattering effects.

The other theory that explains an increase in absorbance due to scattering is based on a change in red blood cell axes. Red blood cells have a biconcave disk shape. During diastole, the major axis of red blood cells is parallel to the blood flow, while during systole it is perpendicular. Therefore the optical path length is longer during systole, which increases absorbance (Moyle, 1994; Webster, 1997). Steinke and Shepherd in 1986 published that scattering effects of light passing through *whole* blood depend on the wavelength of incident light and the oxygen saturation i.e., the presence of oxyhemoglobin (Webster, 1997). The total absorbance has a larger slope than the slope due to the absorbance of hemoglobin following Beer-Lambert's law. Thus, light scattering tends to increase the sensitivity of the photoplethysmograph waveform for detecting changes in absorbance.

1.2.7 Bluetooth®

Bluetooth® is a promising technology eliminating use of cables that connect various personal computing devices and creating new types of smart wireless communications. It is wireless standard and communications protocol primarily designed for low power consumption over short distances (30 feet). Bluetooth® provides automatic synchronization between multiple Bluetooth® devices. Bluetooth® radios use a radio band - Industrial, Scientific, and Medical (ISM) band – between 2.4 and 2.48 gigahertz (Miller).

CHAPTER 2

IMPLEMENTATION OF HARDWARE AND SOFTWARE

In Chapter 1, background research on photoplethysmograph and the underlying physiological systems was discussed in detail. This chapter is dedicated entirely to the discussion of the hardware built to obtain a clean analog PPG signal, and to the discussion of the software for extracting respiratory rate from the digitized PPG signal.

Xpod® module used to obtain the PPG signal in the current ambulatory system is an off-the-shelf patented device. The main objective of the Xpod® module is to provide heart rate and oxygen saturation parameters using the PPG signal. It is difficult to obtain the exact filtering and amplification characteristics of the Xpod® because of propriety issues. The normal heart rate at rest in adults is 60 – 100 beats per minute and during exercise it can reach as high as 200 beats per minute (depending on age) (clevelandclinic.org). It is reasonable to assume that Xpod® might band-limit the PPG signal in the 0.67 – 7 Hz (40 – 420 beats per minute) frequency range to account for both normal and abnormal (tachycardia and bradycardia) heart rates. The normal spontaneous respiratory rate at rest for adults is in the range of 10 – 16 breaths per minute (Chang, 2001), which corresponds to 0.15 – 0.27 Hz. If the Xpod® filter cut-off assumption is held true, the respiratory rate frequencies fall in the stop band, thus, attenuating the respiratory rate related information. Thus, to extract respiratory rate from the PPG signal it is essential to know the exact filtering characteristics of the hardware.

In addition, from previous experiments it was noticed that the resolution of the PPG signal from the Xpod® deteriorated at low blood perfusion levels. Thus, apart from the limitation induced due to BlueSentry® module's input requirement, there are other

issues with the Xpod® module, which can be resolved by constructing a custom PPG hardware. A simplistic block diagram of the PPG hardware designed for this study is provided in Figure 2.1. The filters of the custom PPG hardware were designed keeping the frequencies related to the normal respiratory rate under perspective. 0.1 – 5 Hz was used as cut offs for the filtering circuit. Ideally, the lowest respiratory rate that can be extracted (in the software) is, thus, 6 breaths per minute.

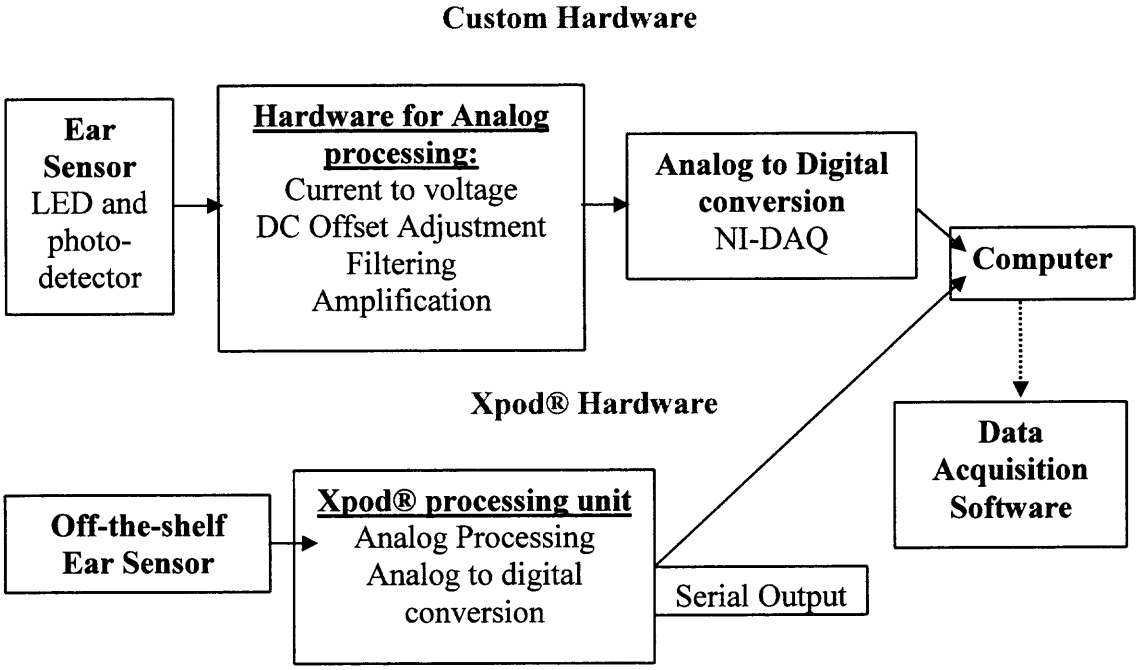

Figure 2.1 Simplistic block diagram of PPG custom hardware and Xpod® Hardware.

National Instrument's LabVIEW® 8.0 software was used for the purpose of applying highly sophisticated digital signal processing tools to obtain respiratory rate from the PPG signal (Figure 2.1). The digitized PPG signal is analyzed using digital elliptic filter in the time domain and power spectrum analysis in the frequency domain, which ultimately defines the respiratory rate detection algorithm. In order to understand

the algorithm accurately, a detailed discussion of the software and its implementation in this thesis is provided in the sections below.

2.1 Discussion of Hardware

This section describes the custom PPG hardware in detail. The PPG sensor designed for this study consists of an infrared light emitting diode (LED) and a photo-detector. The sensor can be placed on any peripheral body parts such as toe, finger, ear lobe or forehead to obtain the PPG signal. Ear and forehead sensors induce the least amount of motion artifact in the PPG signal. However, the blood perfusion in the forehand is less than the ear lobe. The PPG signal obtained from the ear lobe requires less amplification. Considering these factors, an ear lobe sensor was designed for this study. A Staples® paper clip provided as the ear clip sensor housing (Figure 2.2). The spring of the paper clip was replaced with a lesser tension one from one of the unused Nonin® ear clip sensor (Model: 8000Q). The LED and photo-detector were glued to the clip using Duco Cement® on opposite surfaces. Figure shows the ear clip sensor designed for this study:

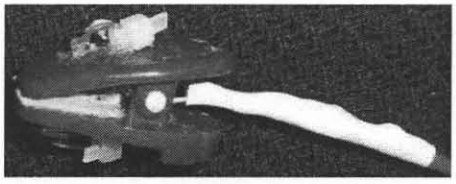

Figure 2.2 Custom ear clip sensor.

Figure 2.3 shows a complete block diagram of the analog processing circuit used for this study. Each of the stages presented in the diagram are discussed in more detail in later sections. The infrared LED, the photo-detector and the passive components such as resistors and capacitors were purchased from an extensive online electronic store

(mouser.com). The transimpedance amplifier, DC offset, inverting amplifier, low pass filter, high pass filter, and notch filter circuits were built using an appropriate set of passive components.

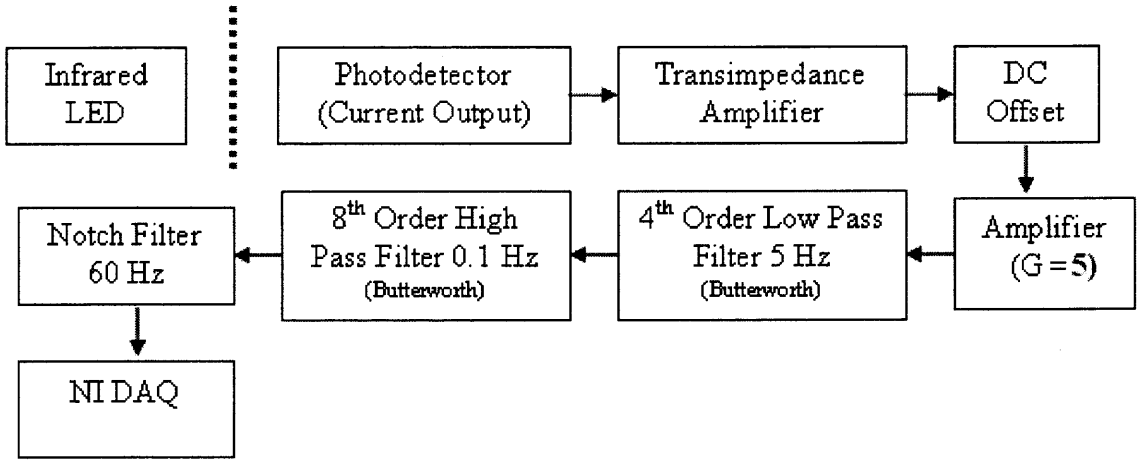

Figure 2.3 Block diagram of custom hardware.

2.1.1 Light Emitting Diode (LED)

As seen in Figure 2.3, the first two components: light emitting diode (LED) and photo-detector form the building blocks of an ear lobe PPG sensor. An LED is a semiconductor diode that allows the current to flow only in one direction while producing light. Emission of light with a particular wavelength (i.e., color) depends on the semiconductor material used to build the LED. LED emits light by a process called electroluminescence. This phenomenon is a result of current flowing through a PN junction in a semiconductor material used to emit light. The LED characteristics such as small packaging, wide range of beam angles, off-the-shelf availability, higher intensity, narrow bandwidth output, easy application, flexible operating temperature range and low cost, make them an ideal choice as a light source for PPG applications.

As mentioned in Chapter 1, infrared LED with 940 nm wavelength is chosen for PPG applications. Features of the LED (Everlight IR91-21C) used for this study are as follows (*Everlight Technical Datasheet,* 2005):

1) Small double-end Package
2) High reliability
3) Good Spectral Matching with Silicon photo-detector (photodiode)
4) Peak Wavelength: 940 nm
5) Spectral Bandwidth ($\Delta\lambda$): 45 nm
6) Operating Temperature: -40 to 85 ^{o}C
7) Beam (View) Angle: 25 Degrees
8) Low Cost – $ 0.30 ea

2.1.2 Photo Detectors

A wide variety of photo detectors are available in the market today, such as photocells, photodiodes, phototransistors, and integrated circuit chips with built-in detectors and other necessary circuitry. For selecting an appropriate photo detector device specifically for photoplethysmography applications, several factors have to be considered.

1. Linearity of the output signal i.e., Linear proportionality of the output signal relative to the intensity of incident light is highly desirable
2. Sensitivity i.e., ratio of the electrical output signal to the incident light
3. Response time i.e., the time it takes in responding to a change in the input
4. Size and Cost (Webster, 1997)

A table comparing each of these factors for photocells, photodiodes and phototransistors is described as follows:

Table 2.1 Electrical Characteristics of Photodiodes, Photocells and Phototransistors for PPG Applications

Electrical Characteristics	**Photodiodes**	**Photo Cells (CdS)**	**Phototransistors**
Available Wavelengths (nano-meter)	200 – 2000	400 – 1100	400 – 700
Linearity	Excellent	Good	Good
Sensitivity	Very Good	Very Good	Very Good
Size	Small	Small	Small
Cost	Low	Very Low	Very Low

http://www.engr.udayton.edu/faculty/jloomis/ece445/topics/egginc/tp4.html

As seen from Table 2.1, the factors such as wavelength availability and linearity of a photodiode make it more suitable for the PPG applications than other sensors. Thus, a photodiode was used for this study.

2.1.2.1 Photodiodes. Photodiodes are semiconductor light detectors that produce current or voltage output depending on the intensity of light incident on the p-n junction in a semiconductor. There are several types of photodiodes available in the market today. These include PN photodiodes, PIN photodiodes, Shottky photodiodes, metal-semiconductor-metal (MSM) photo detectors, and avalanche photodiodes (APD). However, P-I-N diodes have been found to be the most desirable for PPG applications. P-I-N photodiodes have a faster response time than regular diodes. Shottky diodes are primarily used for ultraviolet light detection applications and have response time faster than required for PPG. MSM have lower sensitivity than PIN diodes and are not used. APDs are used for detecting extremely low levels of light as they tend to amplify the noise with the wanted signal. (Webster, 1997; *Photodiode Technical Guide*). They are not used for PPG applications. The silicon based PIN photodiode with 7 mm^2 radiant sensitive area in photoconductive mode is the most desirable choice for PPG applications.

Silicon PIN photodiode from Vishay Semiconductors (BPW24) was used for this study. BPW24 is a high speed and high sensitive PIN diode in a miniature flat plastic package. It has a waterclear epoxy making it more sensitive to visible and infrared radiation. The large active area combined with a flat case gives a high sensitivity at a wide viewing angle (*Vishay Technical Data Sheet,* 2006). BPW24 provides with following features:

1) Large radiant sensitive area: 7.5 mm^2
2) High photosensitivity
3) Fast response times - Rise and Fall times: 100 ns
4) Small junction capacitance
5) Suitable for visible and near infrared radiation
6) Wavelength of peak sensitivity: 900 nm
7) Range of spectral bandwidth: 600 – 1050 nm
8) Wide viewing angle: +/- 65 degrees
9) Low Cost: $ 0.76 ea

This photodiode provided the required radiant sensitive area, range of spectral bandwidth and was suitable for near infrared radiation. These factors made it an ideal choice for this application.

2.1.3 Amplifiers and DC Offset

As presented in Figure 2.3, the output from the sensor assembly is provided to an amplifier and DC offset circuits for further processing. In this section, the architecture and applications of transimpedance and inverting amplifiers, and DC offset circuits are discussed.

The photodiode generates current output and has to be converted into voltage so that filtering, amplification and data acquisition of the PPG signal can be carried out at a later stage. Current-to-voltage amplifiers, also known as transimpedance amplifiers are used for this purpose. The raw PPG signal obtained from any peripheral body site is very low in amplitude. The signal has to be amplified for better resolution characteristics. The raw PPG signal amplitude is in a few milli-volts (after current to voltage conversion) depending on the blood perfusion and scattering characteristics of the ear lobe. In this thesis, an inverting amplifier with a gain of 5 was built to amplify the raw PPG signal. But before the signal can be amplified, a DC offset stage has to be added. The raw PPG signal has the added component called the DC along with the AC component (as

discussed in Chapter 1), which forces the signal to saturate with a gain (amplification) as low as 5. The DC offset circuit is set to normalize the signal to zero, in other words, to cancel out the DC component so that required amplification can be applied.

2.1.3.1 Inverting Amplifier. An inverting amplifier is the most basic op-amp circuitry. The current flowing into the op-amp is considered to be zero because of high input impedance. The positive end of the op amp is connected to ground. So the current flowing through R and R_f is the same. Thus, V_{out}/V_{in} = Gain = $-R_f/R$.

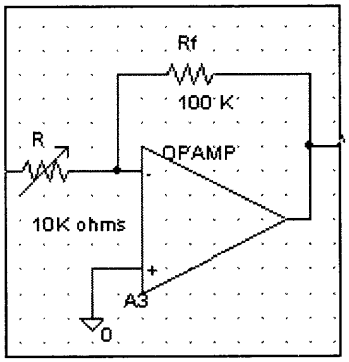

Figure 2.4 Wiring diagram of inverting amplifier.

For this thesis, a potentiometer was used for R, so that the gain on the output signal can be adjusted depending on the PPG amplitude, which changes in relation to the blood perfusion of the site. The values used for R (max pot value = 100 kilo ohms) and R_f are 20k and 100k ohms respectively, which provide a gain of 5. As seen from the equation before, the output of an inverting amplifier is inverted, which was compensated by the DC offset circuit.

2.1.3.2 Transimpedance Amplifier. Transimpedance amplifiers, or current to voltage converters, are amplifiers that convert an input current to an output voltage. The standard transimpedance amplifier configuration is as shown in Figure 2.4.

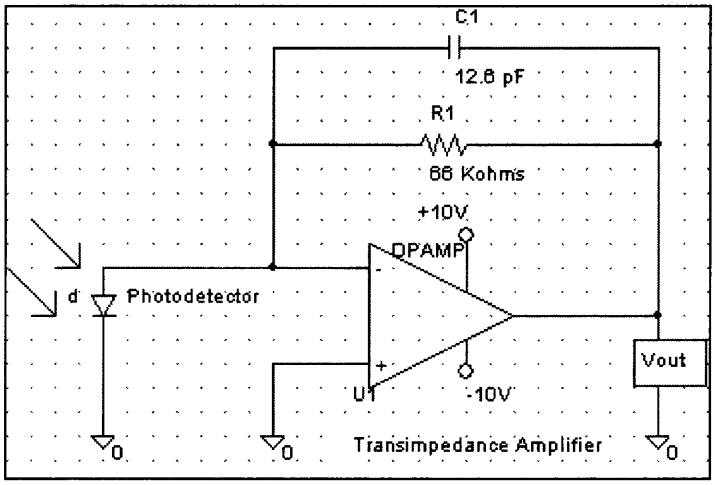

Figure 2.5 Wiring diagram of transimpedance amplifier.

The non-inverting input of the op-amp is connected to ground, which maintains a zero voltage across the photodiode. Current flows through the feedback resistor (R1) and creates a potential difference (voltage) at the output that is proportional to the light intensity. The following equation shows a direct proportionality between the output voltage and the output current of the photodiode related to the light intensity:

$$V_{out} = I_d \times R_1 \tag{2.1}$$

The feedback resistor (R1) is the proportionality constant in Equation 2.1. As the value of R1 is increased, the output voltage increases. Thus, the transimpedance gain depends on the value of the feedback resistor. This resistor value should be as high as possible to minimize noise as it is a dominant source of noise in the circuit. The capacitor in the feedback loop minimizes gain peaking and improves stability (Webster, 1997). Graeme (1992) provided several simplified formulas for determining the feedback capacitance (as cited in Webster, 1997):

$$C_f = \sqrt{\frac{C_I}{2\pi R_f f_c}} \tag{2.2}$$

f_c = unity gain frequency of the op amp
C_I = total input capacitance = photodiode junction capacitance + operational amplifier input capacitance
R_f = feedback resistance
The feedback resistance and capacitance used for this study are as shown in Table:

Table 2.2 Transimpedance Amplifier Feedback Resistance and Capacitance

R_f (Feedback resistance)	66 kΩ
C_f (Feedback capacitance)	10 pF

The feedback capacitance as mentioned in Equation 2.2 was calculated using:

Photodiode junction capacitance = 40 pF
Operational amplifier input capacitance = 1.4 pF
Total capacitance C_I = 41.4 pF

2.1.3.3 DC Offset. The DC offset circuit, as the name suggests, is used to adjust the DC component of a signal to avoid saturation induced due to op-amp and data acquisition card limitations. The raw PPG signal has a DC component (as discussed in Chapter 1), which can force the signal out of the allowed range (NI DAQ 6024E: -10 V to +10V limitation). An op-amp based active circuit was built as shown in Figure 2.6, which is a basic differential amplifier circuit. It adds the two inputs, where a potentiometer at the non-inverting input, is changed to adjust the DC value. The output of DC offset adjustment circuit was inverted.

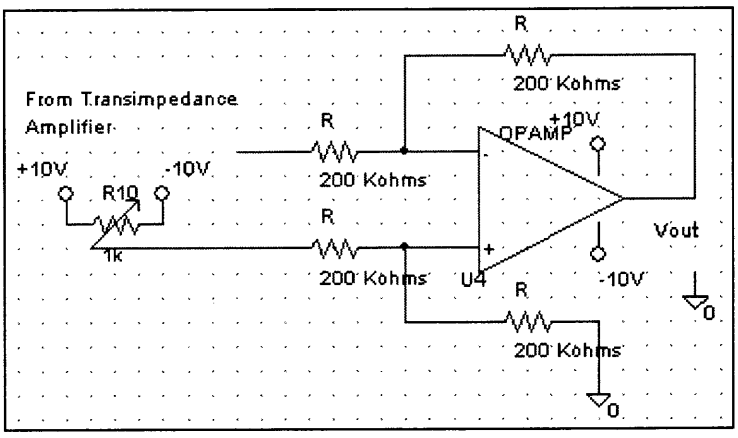

Figure 2.6 Wiring diagram of DC offset adjustment circuit.

2.1.4 Filters

As seen from Figure 2.3, the output from the DC offset circuit was provided to a series of filters in a sequential manner to enhance signal to noise ratio. The continuous raw PPG signal acquired at a body site was contaminated by noise from many sources such as electronic interference (60 Hz), motion artifacts and other unwanted low and high frequency noises. A filter is a circuit that processes signals on a frequency dependent basis i.e. it exhibits a frequency-dependent transfer function called the frequency response. A filter affects not only the amplitude and the phase of an input signal. The magnitude of the frequency response, |H| represents the how the amplitude of the input signal is affected or attenuated by the filter; the angle of the frequency response, $\angle H$ represents the amount of phase shift experienced by the input signal (Franco, 1988).

The high frequencies that constitute a PPG signal is related to the heart rate, while the low frequencies are related to respiration, sympathetic nervous system response and thermoregulation characteristics of the body site under study (as discussed in Chapter 1). As mentioned earlier, the normal respiratory rate in adults is in the range of 10 – 16

breaths per minute. For this study active filters were designed only allowing frequencies in 0.1 – 5 Hz range to pass (ideally), which comprises the 0.15 – 0.33 Hz respiratory rate related frequencies. The higher frequencies (0.33 – 5 Hz) were also included so that heart rate and oxygen saturation parameters could be obtained along with respiratory rate in the future.

Filters, in general, are classified as low-pass, high-pass, band-pass and band-reject. To obtain a clean PPG signal, a 4^{th} order low-pass Butterworth filter with a cutoff at 5 Hz (maximum heart rate 300 beats/minute) and a 8^{th} order high-pass Butterworth filter with cutoff at 0.1 Hz (minimum respiratory rate of 6 breaths/minute) was applied to the raw PPG signal. The order of the high pass and low pass filters were chosen based on previous experiments carried out by Nakajima et al. (1996) who successfully applied a digital filtering technique for monitoring heart rate and respiratory rate from the PPG signal.

A 60 Hz band reject or notch filter was applied to eliminate residual electronic interference after the previous low and high pass filter stages.

Butterworth filter design was chosen mainly because of its simple design, which helped to avoid any type of design related errors. In addition, they maximize the flatness of the magnitude response within the pass band. The response is extremely flat near DC and is somewhat rounded near the cutoff frequency, which was desirable. The attenuation rate of -20n dB/dec is attained in the stopband, where n = the order of the filter. The attenuation rate or transition rate from pass band to stop band of Butterworth filter is not as steep (closer to ideal) as compared to other filters such as Chebyshev, Elliptic, and Bessel (as seen in Figure 2.7). However, to derive respiratory rate from PPG signal, the

flatness of the pass band and stop band was more important than the attenuation rate (Nakajima et al., 1996). Thus, the order of the filters was increased to obtain steeper roll-off.

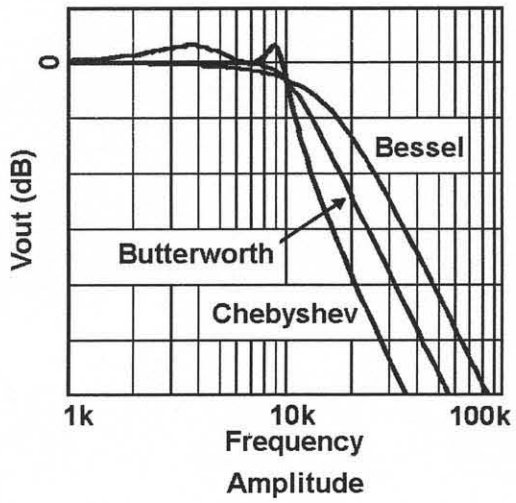

Figure 2.7 Butterworth characteristics compared to Bessel and Chebyshev. http://www-k.ext.ti.com/SRVS/Data/ti/KnowledgeBases/analog/document/faqs/bu.htm

The analog low pass and high pass filters used in this study were unity gain 4th order and 8th order active filters respectively. The design of Butterworth analog filters is a special case of unity gain Sallen-Key filter design.

2.1.4.1 Sallen Key Second Order Low-Pass Filter. The circuit diagram of active low pass Sallen-Key filter is as follows:

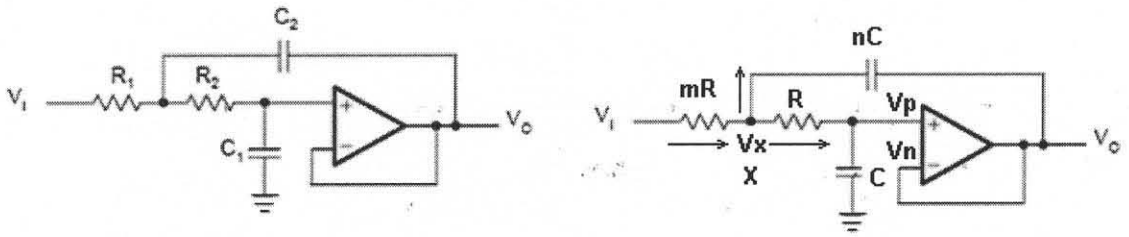

Figure 2.8 Sallen Key low pass filter.

To simplify the circuit design and the algebra, the values of the first RC pair is expressed in terms of the second pair by means of multipliers m and n respectively. Let

R_2 = R then R_1 = mR and let C_1 = C the C_2 = nC. Let the voltage at the node expressed as X in the Figure 2.8 be Vx. Based on the op-amp properties, Vp = Vn. In this case, Vp = Vn = Vo and thus, $V_O = \frac{V_X}{1 + j\omega RC}$. By Kirchoff's current law at node X, $\frac{V_I - V_X}{mR} = \frac{V_X - V_O}{R} + \frac{V_X - V_O}{(1/j\omega nC)}$. Simplifying this equation will give V_I in terms of Vx and Vo. But Vx term can be eliminated by plugging $V_O(1 + j\omega RC) = V_X$ in:

$$V_I = (1 + m + j\omega mnRC)V_X - (m + j\omega mnRC)V_O \Rightarrow V_I = [1 - \omega^2 mnR^2C^2 + j\omega(m+1)RC]V_O$$

Now $\omega = 2\pi f$ so $\omega^2 mnR^2C^2$ can be written as $[2\pi f\sqrt{mn}RC]^2 = \left(\frac{f}{f_O}\right)^2$, where $f_O = \frac{1}{2\pi\sqrt{mn}RC}$. Similarly, in equation the third term can be written in terms of f_O as $j\omega(m+1)RC = \frac{j\left(\frac{f}{f_O}\right)(m+1)}{\sqrt{mn}} = \left(\frac{j}{Q}\right)\left(\frac{f}{f_O}\right)$ where $Q = \frac{\sqrt{mn}}{m+1}$ denoting the resonant peak at the cutoff frequency. Thus the transfer function of this filter can be expressed as:

$$H = \frac{V_O}{V_I} = \frac{1}{1 - \left(\frac{f}{f_O}\right)^2 + \left(\frac{j}{Q}\right)\left(\frac{f}{f_O}\right)} \tag{2.3}$$

If resistor and capacitor values in this filter design are selected such that $Q = 1/\sqrt{2}$ then the Sallen-Key filter configuration provides Butterworth response. This can be obtained by making m = 1 and n = 2 i.e., equal resistances and 2:1 capacitances (Franco, 1988). To obtain this relationship, specific values for the passive components were picked. As mentioned before the low pass filter cutoff value is 5 Hz. Thus,

$$f_O = 5 = \frac{1}{2\pi\sqrt{2}RC}, \text{ when m = 1 and n = 2} \Rightarrow RC = \frac{1}{2\pi\sqrt{2}(5)} = 0.022508$$

$\Rightarrow R = mR = 6.8Kohms$; $C = 3.3\mu F$ and $nC = 6.6\mu F$ fulfills the equation above.

2.1.4.2 Sallen Key Second Order High-Pass Filter. By interchanging the capacitors and resistors in the Sallen-Key low-pass filter configuration gives a high-pass filter:

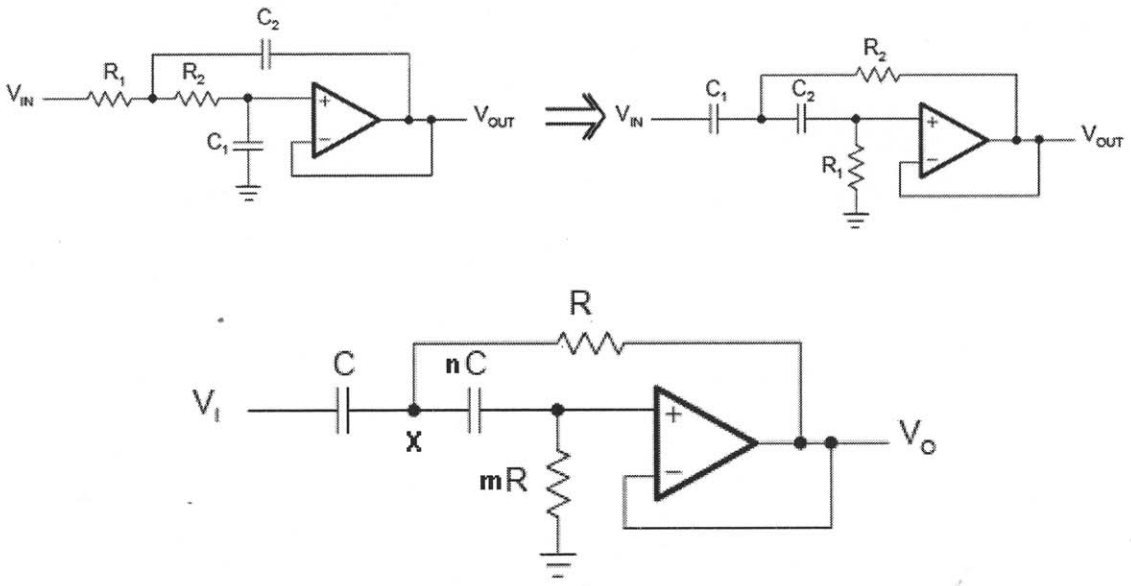

Figure 2.9 Low pass to high pass transition: Second order high pass filter.

As in the low-pass configuration, let R_2 = R then R_1 = mR and let C_1 = C then C_2 = nC. By applying Kirchoff's current law at node X and following the same steps as discussed earlier for the low-pass case, the expression for the transfer function of Sallen-Key high-pass filter is given as:

$$H = \frac{-\left(\frac{f}{f_o}\right)^2}{1-\left(\frac{f}{f_o}\right)^2+\left(\frac{j}{Q}\right)\left(\frac{f}{f_o}\right)}, \text{ where } f_o = \frac{1}{2\pi\sqrt{mn}RC} \text{ and } Q = \frac{\sqrt{mn}}{n+1}. \tag{2.4}$$

If resistor and capacitor values in this filter design are chosen such that $Q = 1/\sqrt{2}$ then the Sallen-Key filter configuration provides a Butterworth response. This can be obtained

by making m = 2 and n = 1 i.e. equal capacitances and 2:1 resistances (Franco, 1988). The high pass cutoff value was chosen to be 0.1 Hz. Thus,

$$f_O = 0.1 = \frac{1}{2\pi\sqrt{2}RC} \text{ , when m = 2 and n = 1 } \Rightarrow RC = \frac{1}{2\pi\sqrt{2}(0.1)} = 1.1254$$

$\Rightarrow R = 100K\Omega$; $mR = 200K\Omega$ and $C = 10\mu F$ fulfills the equation above.

The general Butterworth magnitude response is:

$$|H| = \frac{1}{\sqrt{\left[1+\left(\frac{f}{f_C}\right)^{2n}\right]}} \tag{2.5}$$

, where n = order of the filter and f_C is the cutoff frequency, which represents the -3 dB frequency.

2.1.4.3 Twin-T Notch Filter. Notch filter, which is band-reject type of filter, was used to remove the electrical interference of 60 Hz from the PPG signal. The design of this filter is called the Twin-T mainly because two filters are built in parallel, the upper one is the low-pass type and the lower one is the high-pass type, with the stop bands overlapping. When a low-pass and a high-pass filter are connected in series, a band-pass filter is obtained if the corner frequency of the low-pass device is greater than that of the high-pass device. When connected in parallel, notch filter is obtained if the corner frequency of the low-pass filter is lower than that of the high-pass filter (Franco, 1988).

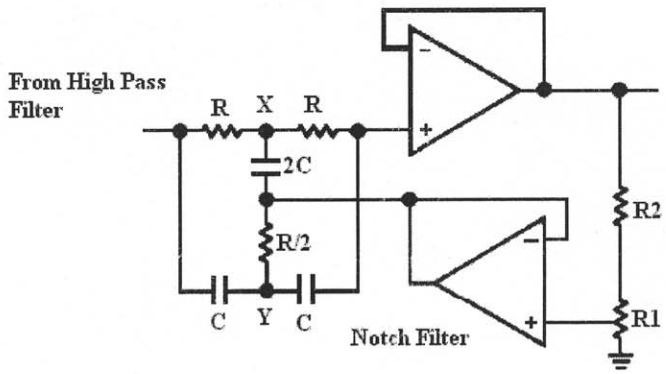

Figure 2.10 Twin-T Notch filter configuration.

Applying Kirchoff's current law at two nodes X and Y, a transfer function H can be derived.

$$H = \frac{1-\left(\frac{f}{f_O}\right)^2}{1-\left(\frac{f}{f_O}\right)^2+\left(\frac{j}{Q}\right)\left(\frac{f}{f_O}\right)}, \text{ where } f_O = \frac{1}{2\pi RC},\ Q = \frac{1}{4(1-K)} \text{ and } K = \frac{R_1}{R_1+R_2} \tag{2.6}$$

For K = 0.95, Q = 5. K = 0.95 can be obtained by taking R1 = 200Kohms and R2 = 10Kohms. For this application, a sharp notch filter, quantified by smaller Q, was not required because the frequencies surrounding the rejection region were not important. R and C can be chosen based on the required band reject frequency, which in this case was 60 Hz. Therefore, $RC = \frac{1}{2\pi(60)} = 0.002654$.

Choosing $R = 560K\Omega$ and $C = 4.7nF$ fulfilled the requirement. Figure A.1 shows the wiring diagram of the overall circuit.

2.1.5 National Instrument's Data Acquisition Card (DAQ)

National Instrument's PCI-6024E was used for converting PPG analog output from the custom PPG hardware into digital. This card is ideal for applications ranging from continuous high-speed data logging to control applications to high voltage signal or sensor measurements when used with compatible software. 6024E DAQ card provides two 12-bit analog outputs, 8 digital I/O lines, two 24 - bit counters, and 16 analog inputs with 16 bit resolution. The maximum sampling rate provided is up to 200 kS/s. It is highly compatible with NI's LabVIEW® software used for this study (*NI's E Series Multifunction DAQ Datasheet,* 2006). One of the analog input channels was used to digitize the analog PPG signal at 75 samples per second.

NI also offers many different high performance shielded cables that have been specifically designed for NI DAQ devices (*NI's DAQ Accessories Selection Guide,* 2007). BNC-2090 rack-mounted BNC terminal block was used to facilitate connecting the analog input channels to the output of the custom hardware.

2.2 Discussion of Software

National Instrument's Laboratory Virtual Instrument Engineering Workbench (LabVIEW®) software provides an easy-to-use intuitive graphical programming background used for varied engineering applications to automate measurement and control systems (ni.com). LabVIEW® version 8.0 was chosen for this study because of its easy access and availability at VA Engineering laboratory. It provides with an intuitive and simple programming experience, especially for data acquisition and processing applications as compared to other programming languages such as Mathwork's

MATLAB, C, and C++. It has the same constructs as other traditional languages such as variables, data types, objects, looping, and sequencing structures as well as error handling (NI.com). The recent versions (8.0/8.2/8.5) of LabVIEW® provide advanced toolkit functionality such as digital signal processing, time series analysis, time-frequency analysis, and multi-rate signal processing. The LabVIEW® package comes with several examples for varied applications that help minimize the learning time significantly.

LabVIEW® consists of two main windows: 1) the front panel and 2) the block diagram. The front panel is a graphical user interface and the block diagram is a wiring diagram, where algorithms are programmed using various LabVIEW® based and/or user defined functions called Virtual Instruments (VIs). For this thesis, the VIs from the signal processing, and serial and analog data acquisition tabs were used.

2.2.1 LabVIEW® Programs

Three separate LabVIEW® programs were developed for this thesis:

1) Data acquisition program
2) Paced breathing program
3) Breathing rate detection program

The data acquisition program was built to acquire the PPG data from both the Xpod® and the custom hardware at the same time to facilitate comparison. Xpod® module outputs data on a serial port of a computer, while the custom hardware outputs an analog signal, which was then converted into digital by NI DAQ 6024E board as described in Section 2.1.5. The block diagram for this program is as follows:

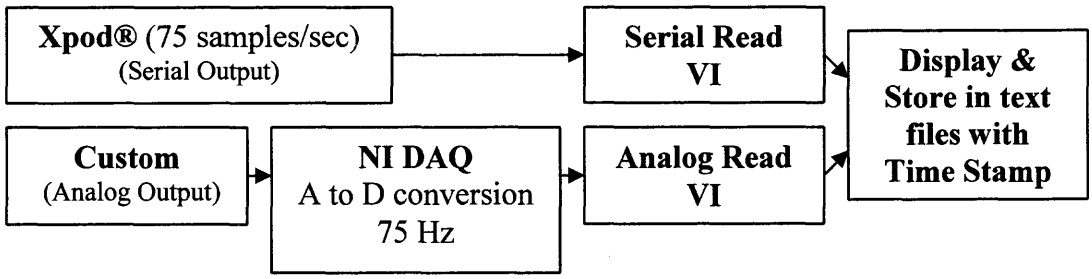

Figure 2.11 Block Diagram of data acquisition program.

The data acquisition program was set so that the sampling rate (75 Hz) of the custom hardware signal matched the rate of the Xpod®. The program facilitated saving the PPG signal obtained from custom and Xpod® hardware to two separate text files with time stamps. The front panel of this program provided controls for inputting subject IDs and to browse to an appropriate location for saving data files. The front panel displayed real-time data from both the sources for visual inspection of data quality.

In the paced breathing program, a sine wave at a known frequencies (corresponding to 6, 9, 12 and15 breaths per minute) was generated and displayed on a vertical process bar plot on the front panel as shown in Figure C.1. The subjects were asked to follow the progress bar to pace inspiration and expiration, i.e. an entire cycle of respiration at 6, 9, 12 and 15 breaths per minute. The subjects were provided with 80 seconds per activity: 20 seconds to practice, and data was recorded in the last 60 seconds. The program displayed a counter that kept track of the number of seconds passed, for subjects' convenience. When the counter reached 60 seconds, it informed the subjects that recording has started by turning the Recording indicator red.

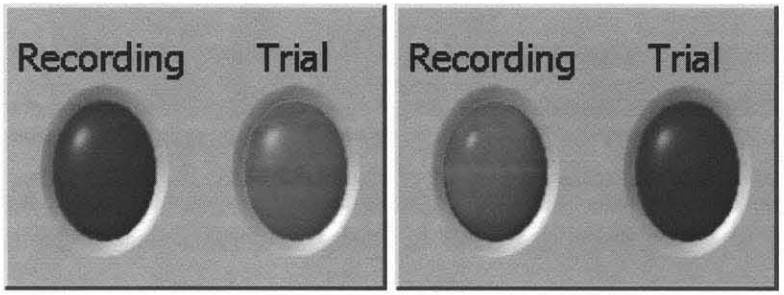

Figure 2.12 Front Panel indicators for subjects' convenience.

The wiring diagram (block diagram) of the paced breathing program is provided in Figure C.2. The reasons for choosing this particular paced breathing rates and the experiment setup of the study are discussed in detail in Chapter 3.

The breathing rate detection program implemented the algorithm for deriving respiratory rate from the PPG signal for 60 seconds data blocks. This program used predefined LabVIEW® VIs for filtering the PPG signal using digital band-pass elliptic IIR filter in the time domain, and autoregressive (AR) modeling techniques (in the frequency domain) for determining the power spectrum of the filtered signal.

This program consisted of multiple stages as shown in the block diagram in Figure 2.12, D.1, D.2, and D.3. The numbers 1, 2, 4A, 4B, 4C, 4D, 4E and 4F in Figure 2.12 correspond to the sections in the breathing rate detection program presented in Appendix D. Each stage performed a different task such as opening the saved data files (Xpod® or Custom data), displaying the original data, application of IIR elliptic band-pass filter, displaying the filtered data, and using the filtered data to obtain the power spectrum (as shown in Appendix D):

1) Section 1: Open and display stored files (Xpod® and Custom data)
2) Section 2: Application of Elliptic IIR filter
3) Section 4A: Downsample filtered signal to get rid of high frequencies
4) Section 4B – 4F: Applying AR modeling technique

A detailed view presenting the signal flow in the detection algorithm is as shown in the Figure 2.13. Each of these sections is described in more detail in the following sections.

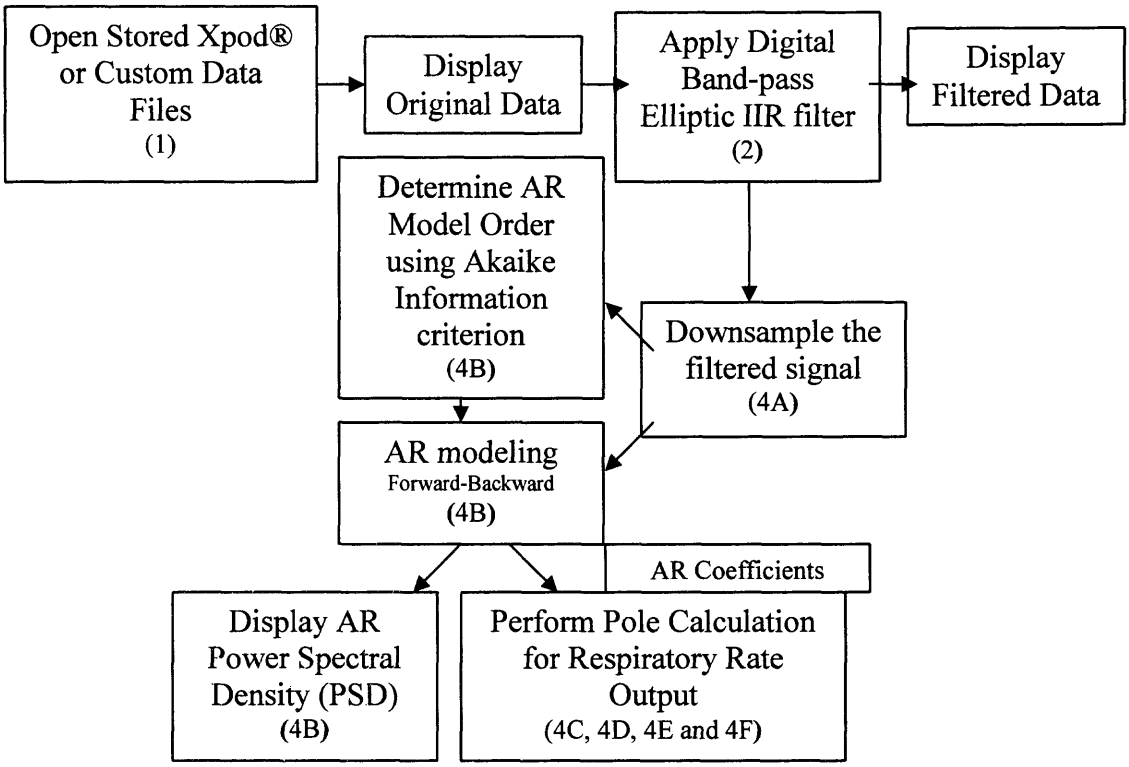

Figure 2.13 Block diagram of breathing rate detection algorithm.

The power spectrum was generated by applying AR modeling technique using Akaike information criterion for model estimation. The last stage was further divided into sub-sections as the AR technique required multiple processing stages (Section 4 in Appendix D).

As shown in the block diagram, the first step was to open stored data files. These were opened using LabVIEW® based Open/Create/Replace File.vi and Read from Text File.vi. Extra data points at the end were discarded if the detected size of the opened file was more than 4500 samples (75 Samples/Seconds* 60 seconds), which corresponds to a

section of 60 seconds. The data was then normalized using Normalize.vi function using the detected mean and standard deviation values. The normalized data was then displayed on a waveform on the front panel. The wiring diagram for this stage is presented in Figure D.1 (Section 1). This step was followed by the application of digital elliptic filter to the input PPG signal.

To understand the detection algorithm systematically, it is essential to first discuss the properties of elliptic band-pass filter and AR modeling techniques in detail.

2.2.1.1 Digital Infinite Impulse Response Elliptic Filter. A LabVIEW®-based elliptic IIR band-pass filter is applied to the stored custom PPG signal for extracting respiration signal. Elliptic filters offer steeper roll-off characteristics compared to the Butterworth or Chebyshev filters, but are equiripple in both the pass and stopbands. Based on trial and error method, elliptic filters consistently showed better performance than Butterworth or Chebyshev with the lowest order. The better performance of elliptic filters can be justified as it provides the sharpest transition between the passband and stopband.

For this thesis, an elliptic filter with bandpass filter setting is used to eliminate the effect due to DC offset and to obtain a low frequency signal corresponding to RIIV signal (Nilsson et al., 2003). The specifications of the bandpass filter are: low cutoff = 0.075 Hz, high cutoff = 0.45 Hz, passband ripple = 0.1 dB, stopband ripple = 80 dB and order = 12. These specifications are selected based on trial and error method. The range 0.075 – 0.45 Hz corresponds to 4.5 – 27 breaths/minute. Stringent filter cut-offs are not applied considering the non idealness of digital elliptic filter.

2.2.1.2 Autoregressive Modeling (AR) Method. AR modeling has been used in various applications including classification, data compression, feature extraction, and pattern recognition of various biomedical signals such as ECG, electroencephalogram (EEG), PPG, blood pressure waveform, heart rate etc. AR modeling has been extensively used to model heart rate variability (HRV) and for *power spectrum estimation* of various other biomedical signals. AR methods are the most widely used modeling methods for power spectral estimation associated with biomedical signals (Akay, 1994). The main advantage of AR modeling is in its simplicity. In addition, it is highly suitable for real-time ambulatory monitoring (Acharya et al. 2007, p. 210).

A power spectrum defines the energy distribution of a time series in the frequency domain, where energy being a real-valued quantity, does not contain phase information. As time series may contain non-periodic signal components, the power spectrum of a times series is considered to be a continuous function of frequency. A series of discrete frequency bins quantifies the continuous characteristic of the frequencies in the power spectrum proportional to the frequency interval (analogous to the time domain analog to digital conversion feature). The power spectrum is divided by the size of the frequency interval (non-periodic) to eliminate its dependence on the frequency interval. This process is called normalization and the output is called the power spectral density (PSD) function. The PSD measures the signal power per unit bandwidth for a time series in $Volts^2/Hz$, assuming an input signal in volts driving a 1 ohm load (*NI Time Series Analysis Tools User Manual*).

AR modeling is a parametric method for estimating the PSD of a time series i.e., model parameters from the time series have to be obtained before PSD estimation. The

estimation of these parameters is a well established topic. They are computed by using algorithms such as least squares, Burg, Geometric, Forward-Backward and Yule Walker methods, which are based on solving linear equations of the system. In order to extract features from the raw time-varying biomedical signals, a number of power spectral estimation techniques, including the parametric methods, have been developed and compared to the standard fast Fourier transform (FFT) methods (Ubeyli et al., 2007).

The main *generic* differences between the parametric and non-parametric methods are the use of data windowing and difference in variances. Non-parametric (FFT and Welch) methods require a use of windowing for a smooth truncation of the side frequencies, which results in distortion of estimated PSDs due to window effects. However, the estimated PSD obtained this way is not subjected to false frequency peaks and spectral leakage effects. In contrast, parametric methods do not use windowing but PSD obtained using these methods may contain false peaks, if the assumed model is wrong. PSDs obtained using parametric methods are less biased and possess a lower variance than PSDs estimated with non-parametric methods (LabVIEW® Manual). According to Ubeyli et al. (2007), the FFT method is based a finite set of data, where the frequency resolution is equal to the spectral width of the window length N, which is approximately 1/N. The windowing effect smoothens the estimated spectrum and thus the FFT method cannot resolve details in resultant spectrum that are separated by less than 1/N in cycles per sampling interval (spectral resolution limit). The model-based estimates (parametric method) are not affected by any smoothening and spectral leakage effects and thus provide a better frequency resolution (Ubeyli et al., 2007).

Ubeyli et al. (2007) examined PSD estimates of several biomedical signals such as PPG, ECG and EEG using FFT and the least squares AR methods. These PSD methods were compared to quantify 1) frequency resolution and 2) the effectiveness in feature extraction for the PPG, ECG and EEG signals (Ubeyli et al., 2007). Their study concluded that the PSD obtained using classical methods had larger variance and that the performance of the least squares AR method was superior to the FFT method. The FFT method showed low spectral resolution and was not found appropriate to evaluate PSDs of the PPG, ECG and EEG signals. The performance of the least squares AR method is extremely valuable for extraction of the features. Thus, AR model was used for estimating the PSD of the digitally filtered signal in this study.

2.2.1.3 Principle of Operation. AR modeling techniques enable to predict the current values of a time series, x_t based on the past values x_{t-1}, x_{t-2},..., x_{t-n} plus a prediction error, e_t. The value *n* is the number of past values used to predict the current value, which is the AR model order. An AR model with order n is described in Equation:

$$x_t + a_1 x_{t-1} + a_2 x_{t-2} + \ldots + a_n x_{t-n} = e_t \tag{2.7}$$

1, a_1,a_2, ..., a_n are the AR coefficients and e_t is the prediction error, which is white noise with a mean of zero. The z-transform of Equation provides a concise representation as described in Equation:

$$A(z)\, X(z) = E(z) \tag{2.8}$$

A(z) is the AR transfer function, which is defined as follows:

$$A(z) = 1 + a_1 z^{-1} + a_2 z^{-2} + \ldots + a_n z^{-n} \tag{2.9}$$

In AR modeling, the time series is considered to be the response of a linear system with a white noise as input (mean = 0). In this case, an AR model represents the linear system with the model prediction error e_t as the white noise input (Figure 2.14).

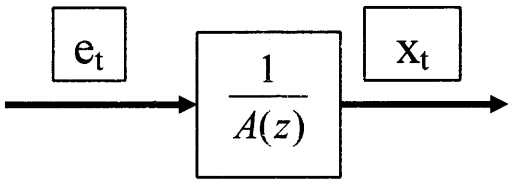

Figure 2.14 AR transfer function.

H(z) = (1/A(z)) represents the transfer function of a system that generates the time series x_t. The AR model is an all-pole model as it does not have zeroes as seen from Equation 2.10. The poles of this model can be obtained by factorizing the denominator polynomial.

$$H(z) = \frac{1}{A(z)} = \frac{1}{\sum_{k=1}^{p} a_k z^{-k}} \tag{2.10}$$

Thus, in the AR method, data can be modeled as output of a causal, all-pole, discrete filter (*A(z)*) whose input is white noise (error). The resultant AR coefficients can be used to estimate the dynamic characteristics of the system that generates the time series (Akay, 1994; *NI Time Series Analysis Tools User Manual,* 2005).

The selection of the model order in the AR spectral estimator is an important subject. If the order is too low, there will be no specific peaks in the spectrum and the frequency details of the signal can not be identified. If the order is too high, false peaks may contaminate the frequency spectrum output (Ubeyli et al., 2007). The optimum AR model order value is selected based on many well-established criteria such as Akaike information, Phi criterion, Bayesian information, etc.

For this study, Akaike information criterion (AIC) was selected as it was suggested by Ubeyli et al. (2007) In addition, it was also found to be more efficient than other criterion for PPG data based on trial and error method. This criterion is a weighted estimation error based on the unexplained variation of a given time series with a penalty term when exceeding the optimal number of parameters to represent the system. For the AIC, an optimal model is the one that minimizes the following equation:

$$\mathrm{AIC} = V_n\left(1+\frac{2n}{L}\right) \tag{2.11}$$

Where L = number of data points in a time series, n = model order and Vn = prediction error. For this thesis, Forward-Backward predication method, which is based on the least squares AR method was used for estimating the AR coefficients (a_k).

2.2.1.4 Breathing Rate Detection Algorithm using the AR model. As mentioned before, the breathing rate detection algorithm was applied using LabVIEW® 8.0 platform using functions from Time Series Analysis (TSA) - Advanced Signal Processing Toolkit. AR model with Akaike information criterion and Forward-Backward method, variant of Least Squares method, was used to quantify the power spectral density (PSD) function of the input signal. This program was designed in a sequential manner to avoid any type of confusion, where analysis is based on shared variables. Figure 2.11 shows a simplified block diagram to elucidate the breathing rate algorithm.

An advanced signal processing function - TSA Resampling.vi - was used to decimate or downsample the signal to enhance the frequency resolution. For a 60 seconds block, the signal was resampled at 1 Hz. The signal was normalized to eradicate the DC offset, which appears at the zero frequency in the power spectrum density waveform (Figure D.2 Section 4A).

The next section, as shown in Figure D.2 Section 4B, of the program uses the toolkit based function (TSA AR Modeling Order.vi) to obtain an optimum AR model order using Akaike information criterion and limiting the order in 1-15 range. TSA AR Modeling.vi was used to estimate the AR model of the input time series using the Forward-Backward method. TSA AR Spectrum.vi was used next to compute a single-sided power spectral density (PSD) waveform of the input time series based on the output of the TSA AR Modeling.vi function. The frequency value corresponding to the maximum magnitude of PSD function was computed based on the frequency interval.

The next section, as shown in Figure D.2 Section 4C, factorized the pole polynomial from the AR coefficients to obtain the magnitude and angular (frequency) component. The poles occur in complex conjugate pairs and define spectral peaks in the power spectrum of the signal, where higher magnitude poles correspond to higher magnitude peaks. The frequency of each spectral peak is given by the phase angle of the corresponding pole, such that the phase angle (theta) of a pole at frequency f is defined in the Equation (T = sampling period, f is pole frequency (Fleming et al., 2007).

$$\text{Theta} = 2\ \text{pi}\ f\ \text{T} \tag{2.12}$$

The Polynomial Roots.vi and Complex to Polar.vi were used to factorize the polynomial and to convert complex roots into their subsequent components (magnitude and angle (theta)) respectively. The unit of theta obtained this way was radian and had to be converted into hertz (Figure D.3 Section 4F).

The next step, as shown in Figure D.3 Section 4D, was to find the respiration group by setting the limit for the frequency component; this step was essential as it facilitated in separating the high frequency components corresponding to the heart rate

information, and the low frequency components corresponding to the respiratory rate information. The limits used for this study were 5 as the minimum and 17 as the maximum breaths per minute. The In Range and Coerce.vi was used to limit its output based on the range provided (1.7804 and 0.5236 radian). A new array called Respiration theta was created to store the values that appear in the required range. The analysis in the following stages was based on 'Respiration theta' values only.

An elimination criterion had to be applied to the cases where the respiration group contained more than one theta value (corresponding to the breathing rate frequency). This criterion was based on the maximum value detected from the PSD waveform as shown in Figure D.2 Section 4E. The estimated respiratory rate (final output) was provided by converting the theta value, which was in radians, into breaths per minute using following equation (T = sampling period = 1/75 = 0.0133 seconds) (Figure D.3 Section 4F):

$$\text{Respiratory Rate } (f_{60}) = \left(\frac{theta}{2\pi T}\right) \times 60 \text{ (breaths per } minute) \tag{2.13}$$

This rate was displayed on the front panel as the final output of the algorithm. The PPG signals obtained during the experiment (Chapter 3) for paced breathing were inputted into the breathing rate program and the estimated respiratory rate values were recorded for each subject. A detailed discussion of the experiment setup and protocol is provided in Chapter 3.

CHAPTER 3

EXPERIMENT SETUP AND RESULTS

In Chapter 2, the hardware and software designed for this study were discussed in detail. This chapter is divided into two sections where the first section discusses the setup of the experiment and the protocol for acquiring data. The second section provides the results obtained from the setup, and the statistical analyses of data, and the plots.

The protocol was developed by considering three important concerns related to 1) the custom ear sensor reliability, and 2) the custom hardware analog processing, in an ambulatory setting and 3) breathing rate detection program accuracy. As seen in Table 3.1, the first half of the protocol was designed to simulate various situations that can induce motion artifacts such as head and body movements, in an ambulatory setup during the HEMI study. The second half was designed to measure the accuracy of the breathing rate detection algorithm. The individual was asked to pace breathing at 6, 9, 12 and 15 breaths per minute with a help of LabVIEW®-based paced breathing program (as discussed in Chapter 2; Appendix C) three times in random order. The experiment setup and the protocol are discussed in more detail in the following sections.

In order to understand the results in more detail, they are discussed in two sub-sections. The first section will deal with the verification of filters used in the custom PPG analog processing circuit. In addition, the PPG signal obtained from both the custom and Xpod® hardware during different activities will be quantified for motion artifacts using signal to noise ratio (SNR) and Pearson correlation coefficient (R) measurements. The second section verifies the efficiency of the software in detecting the respiratory rate using several statistical analyses.

3.1 Experiment Setup and Protocol

The protocol for data collection is provided in Table 3.1. In order to check the reliability of the custom ear clip sensor in an ambulatory setup, it was important to obtain data by simulating certain situations that can present motion artifacts such as changes in incident ambient light and movement itself. The Up/Down, and Left/Right head movements are hypothesized to present artifacts because of a change in the ambient light incident on the detector and also due to a slight change in the placement of the ear sensor clip with movement. Talking also is hypothesized to induce slight changes in the ear clip sensor placement. Head movements are believed to be a direct cause of motion artifacts, while body movements such as walking and hopping are considered to be an indirect cause. The body movements are hypothesized to cause motion artifacts because the wires attached to the sensor change the ear clip sensor placement as the individuals walk or hop with the wires hanging on their sides. Hopping activity was included in the protocol to check the extremes of both the hardware. The paced breathing activities were included in the protocol to check the reliability and accuracy of the breathing rate detection algorithm.

System testing for the proof of concept was done on one individual at NJIT. The custom ear sensor was placed on the left ear, and the Nonin® ear clip sensor on the right ear, with LED on the top surface (Figure 3.1). The individual was seated on a chair as close to the breadboard based analog processing circuit as possible and facing a laptop computer with paced breathing program running. The data acquisition program was placed on a separate computer to allow viewing the data real-time by the operator only. The individual was asked to sit without movement for about a minute, while the operator

checked for the signal quality and visibility. If there were any problems, the individual was asked to remove the sensor and place it back on after a few seconds.

Table 3.1 Protocol

Individual ID		
Normal Breathing No movement (1 min)		
Sitting		
Head Movement Normal Breathing (1 min)		
Up & Down		
Left & Right		
Talking		
Body Movement Normal Breathing (30 sec)		
Walking		
Hopping		
Paced Breathing (Breaths/min) 3 times in random order		
6	12	9
9	9	15
12	15	12
15	6	6

As described in Table 3.1, the paced breathing rates were repeated three times in a different order each time, in order to reduce possible effects of fatigue etc. The individual was asked to perform each task for 80 seconds: 20 seconds for practice and last 60

seconds were recorded. During the body movements, the individual was asked to keep the head movements to the minimum. For the paced breathing part of the setup, individual was asked to keep as still as possible to obtain a clean PPG signal to check the reliability of the detection program in a controlled fashion.

Figure 3.1 Experiment setup.

3.2 Results

A PPG module, which includes a sensor and an analog processing unit, designed for this study was required to match the characteristics of Xpod® module. Also it was designed to enable a control over the sampling rate, filtering characteristics and quantization/resolution levels of the PPG signal.

The custom PPG hardware developed for this study included an analog filtering stage to obtain a clean PPG signal within 0.1 – 5 Hz frequency range. In the following section, 1) Bode plots are presented to verify the cut offs of the custom filters. 2) In addition, the PPG signals obtained from both the hardware (custom and Xpod®) are compared. The verification of the custom PPG hardware was performed by comparing the PPG signal obtained from both the hardware at the same time, for different types of activities (as discussed in the protocol). 3) Lastly, the quantization levels of the PPG signal (obtained from the both hardware) is compared.

The next section discusses the results obtained to verify the efficiency of the breathing rate detection algorithm.

3.2.1 Hardware Verification Results

3.2.1.1 Verification of Filters. The filters designed for this study were tested by developing a frequency response (Bode plot) profile using a known signal - a sine wave - at varying but known frequencies as an input to the circuit. The frequency magnitude of the input sine wave signal was compared to that of the output signal after each filter stage. A ratio of output (Vout) and input magnitude in volts (Vin) was calculated and converted into decibel units (20*log10(Vout/Vin)) to quantify the change due to filtering. The frequency response Bode plots for the Butterworth 8th order high pass filter and the 4th order low pass filter are provided in Figure 3.2, and that for the 60 Hz notch filter is provided in Figure 3.3.

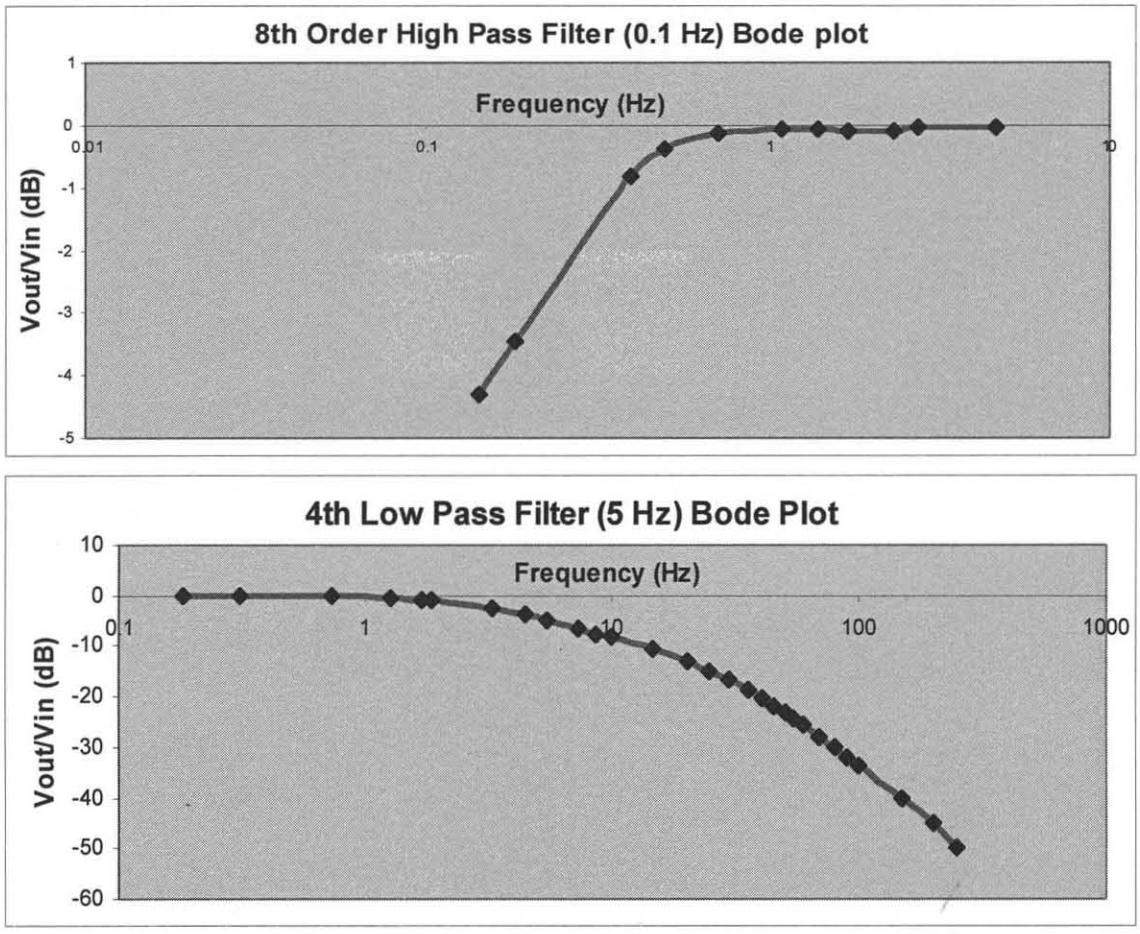

Figure 3.2 8th order Butterworth high pass (top) and 4th order low pass filter Bode response (bottom).

The Butterworth 8th order high pass filter and 4th order low pass filter responses, as shown in Figure 3.2, confirmed that the response for Butterworth filter is flat near DC (zero frequency) and that it is rounded near the cut-off frequencies, which in this case are 0.1 Hz and 5 Hz respectively. It was difficult to find a function generator that could produce frequencies less than 0.1 Hz. Therefore, the test was performed using the lowest frequency setting possible on the function generator (0.143 Hz). The input frequencies and the corresponding V_{out}/V_{in} magnitude ratios for both the filters are provided in the Tables 3.2 and 3.3 below:

Table 3.2 Sine Wave Frequencies used to Test 8th Order Butterworth High Pass Filter Hardware and the Corresponding V_{out}/V_{in} Magnitude Ratios

Dialed Frequency (Hz)	Measured Frequency (Hz)	Magnitude Ratio	Mag Ratio (dB)
0.143	0.1	0.608	-4.32
0.182	0.2	0.672	-3.45
0.4	0.4	0.909	-0.83
0.5	0.5	0.956	-0.39
0.714	0.7	0.985	-0.13
1.11	1.1	0.991	-0.08
1.4	1.4	0.992	-0.07
1.71	1.7	0.988	-0.10
2.33	2.3	0.989	-0.10
2.75	2.7	0.995	-0.04
4.67	4.7	0.996	-0.03

Table 3.3 Sine Wave Frequencies used to Test 4th Order Butterworth Low Pass Filter Hardware and the Corresponding Magnitude V_{out}/V_{in} Ratio

Dialed Freqeuncy (Hz)	Measured Frequency (Hz)	Magnitude Ratio	Mag Ratio (dB)
0.182	1.00	0.017	0.182
0.308	0.99	-0.061	0.308
0.727	0.98	-0.167	0.727
1.273	0.94	-0.510	1.273
1.7	0.91	-0.829	1.7
1.85	0.89	-0.963	1.85
3.3	0.74	-2.627	3.3
4.5	0.63	-3.944	4.5
5.5	0.56	-5.005	5.5
7.3	0.47	-6.576	7.3
8.7	0.42	-7.618	8.7
10	0.39	-8.223	10
14.7	0.29	-10.663	14.7
20.3	0.22	-12.995	20.3
25.1	0.18	-14.894	25.1
30	0.15	-16.654	30
35.7	0.12	-18.636	35.7
41	0.09	-20.445	41
45.6	0.08	-21.830	45.6
50.7	0.07	-23.223	50.7
55	0.06	-24.308	55
60	0.05	-25.63	60
70	0.04	-27.959	70
80	0.03	-30.061	80
90.4	0.02	-32.041	90.4
100.5	0.0205	-33.765	100.5
150	0.0097	-40.220	150
200	0.0055	-45.224	200
250	0.0033	-49.682	250

The band-reject filter used to remove the 60 Hz electrical noise from the PPG signal was tested in a similar fashion. The frequency response curve in Figure 3.4 shows that the ratio of the magnitude (V_{out}/V_{in}) reduced gradually in the range of 25 – 70 Hz. Such a broad range demonstrated that the band-reject filter did not provide a sharp cut off at 60 Hz, which confirmed that Q was, in fact, a high value. As mentioned in Chapter 2, a

sharp notch filter (smaller Q) was not required because the frequencies higher than 5 Hz are considered meaningless for this application.

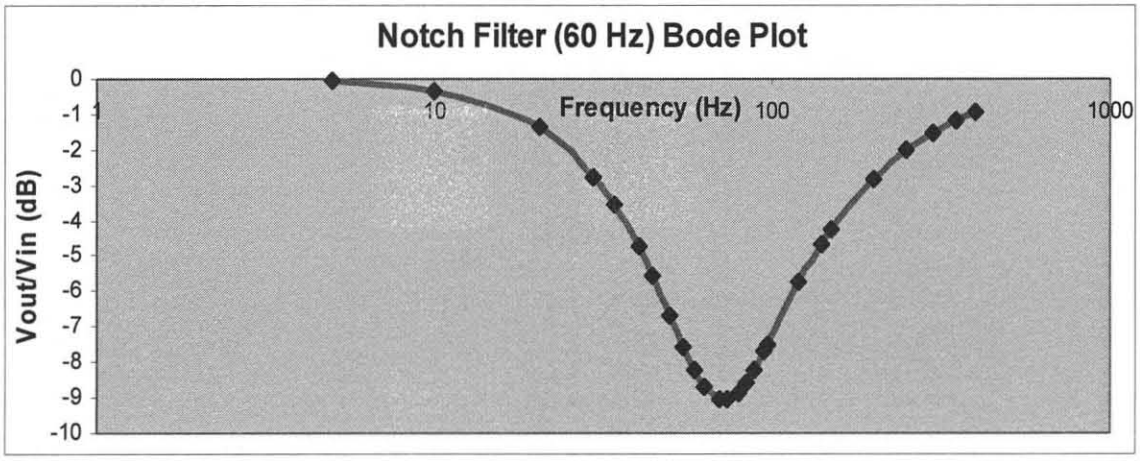

Figure 3.3 60 Hz notch filter bode plot.

The Table 3.4 providing the input sine wave frequencies and the corresponding magnitude V_{out}/V_{in} ratio is as follows:

Table 3.4 Sine Wave Frequencies used to Test Twin-T Notch Filter Hardware and the Corresponding Magnitude V_{out}/V_{in} Ratio

Measured Frequencies (Hz)	Magnitude Ratio	Mag Ratio (dB)
5	0.99	-0.09
10	0.96	-0.37
20.5	0.85	-1.38
29.8	0.73	-2.76
34.2	0.66	-3.57
40.4	0.58	-4.72
44.5	0.53	-5.56
50.1	0.46	-6.69
55.0	0.42	-7.56
59.3	0.39	-8.20
63.6	0.37	-8.71
69.9	0.35	-9.04
74.5	0.35	-9.07
79.7	0.36	-8.90
84.8	0.37	-8.57
89.2	0.39	-8.25
95.3	0.41	-7.70
97.6	0.42	-7.51
120.8	0.52	-5.76
140.4	0.58	-4.69
150.0	0.61	-4.26
200	0.721	-2.84
250	0.791	-2.04
300	0.838	-1.53
350	0.87	-1.21
400	0.894	-0.97

3.2.1.2 Verification of PPG Signal Quality During Activities. Verification of signal quality was performed on the PPG signals obtained during different activities (in the protocol). The data quality during activities was verified by comparing PPG signals with the no movement ones. The activity: *sitting* was used as a standard (no movement case) to compare the rest. Below, plots for the individual are shown for each of the six activities (mentioned in the protocol). Data were collected on both sets of hardware

simultaneously. Following these plots is an analysis of the signal to noise ratio and correlation coefficient between data collected on the two sets of hardware.

On each plot below, blue represents PPG signals from the custom hardware and pink is from the Xpod® hardware.

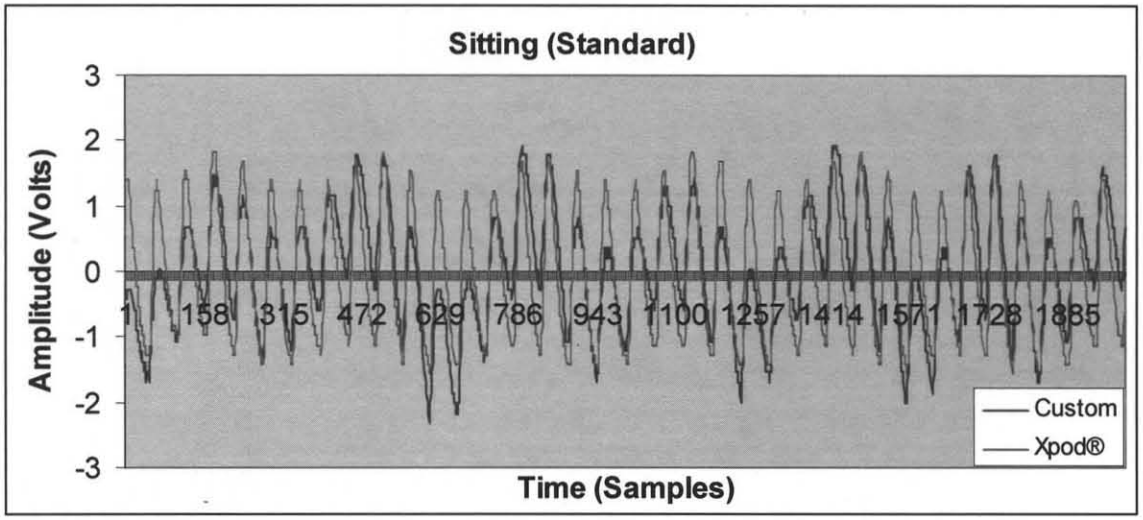

Figure 3.4 Raw PPG output from custom and Xpod®: Sitting activity (pink – Xpod®; blue – Custom).

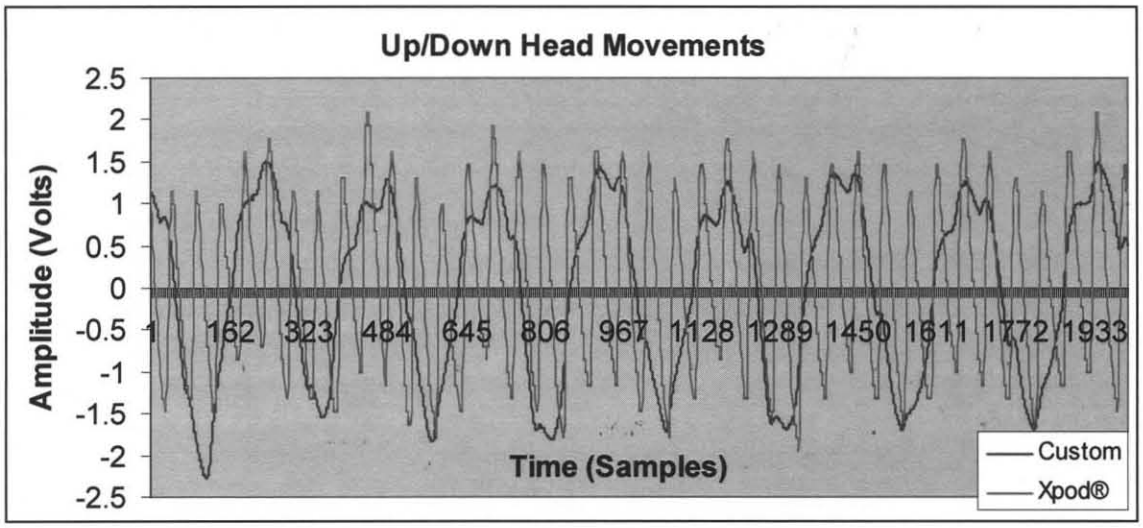

Figure 3.5 Raw PPG output from custom and Xpod®: Up/down head movements (pink – Xpod®; blue – Custom).

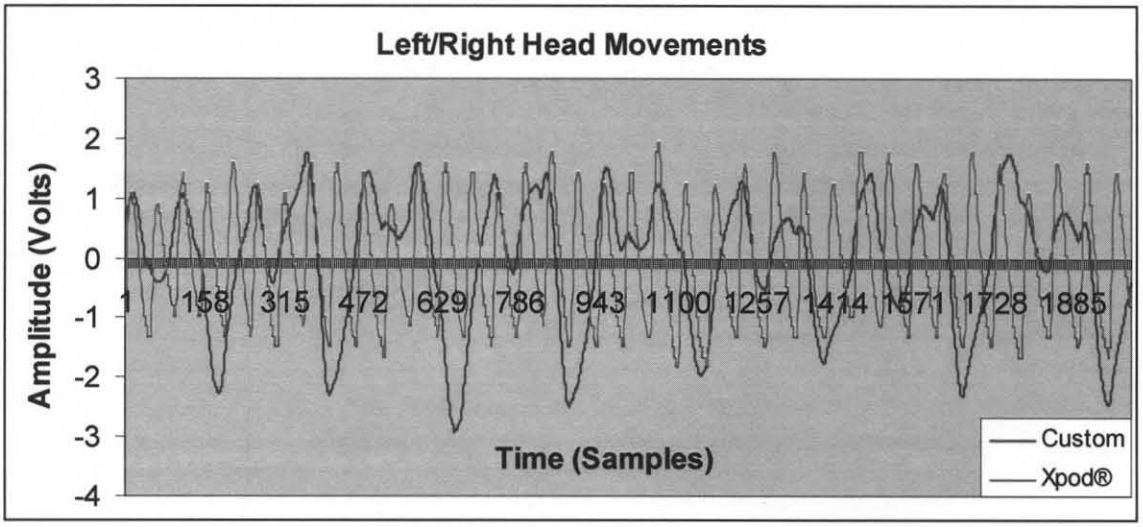

Figure 3.6 Raw PPG output from custom and Xpod®: Left /right head movements.

The head movement activities (Figure 3.5 and 3.6) induced low frequency noise, which was more pronounced in custom PPG case than the Xpod®.

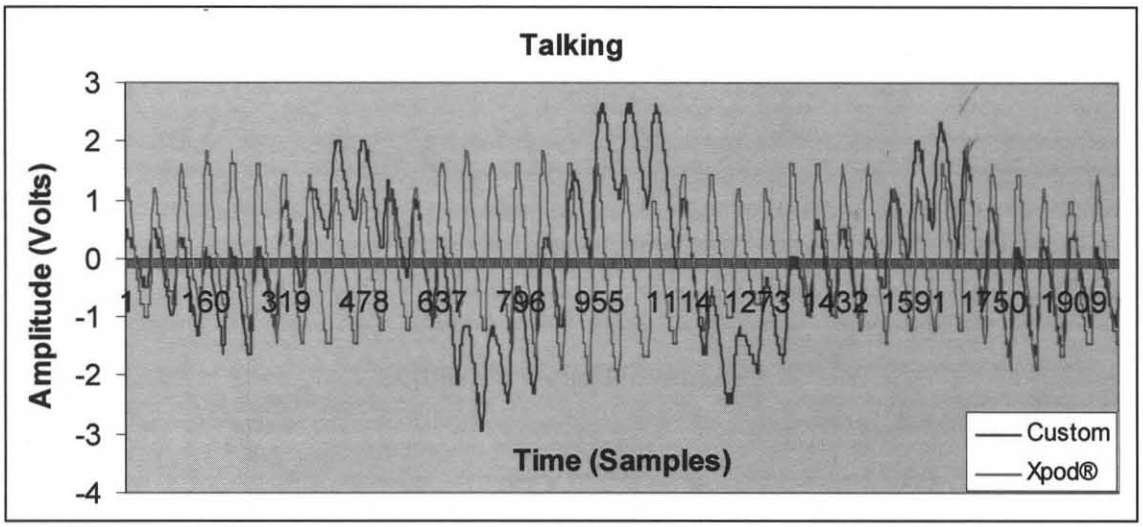

Figure 3.7 Raw PPG output from custom and Xpod®: Talking activity.

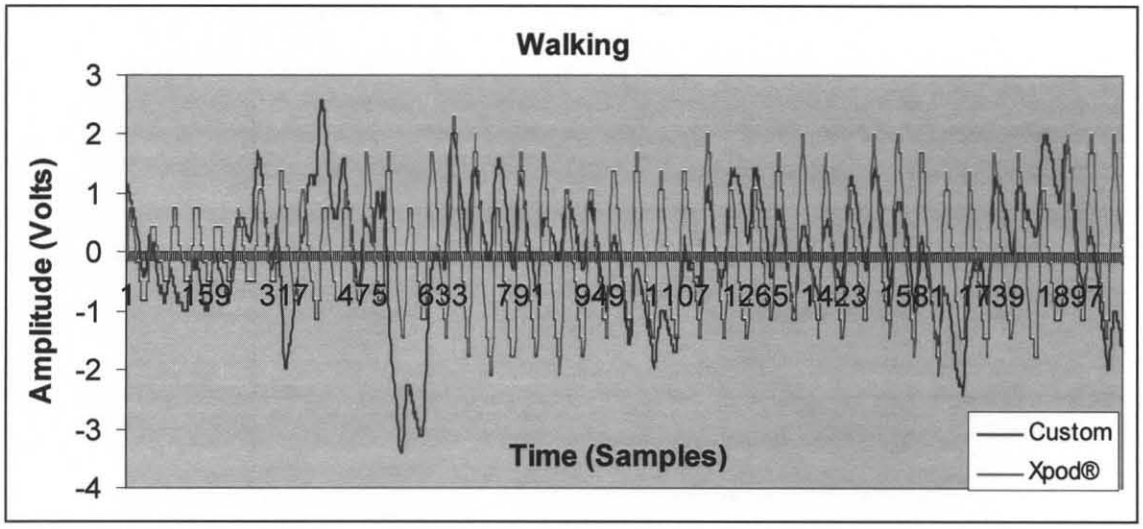

Figure 3.8 Raw PPG output from custom and Xpod®: Walking activity.

As seen from the Figure 3.7 and 3.8, talking and walking activities did not affect the custom PPG signal as much as the head movements did.

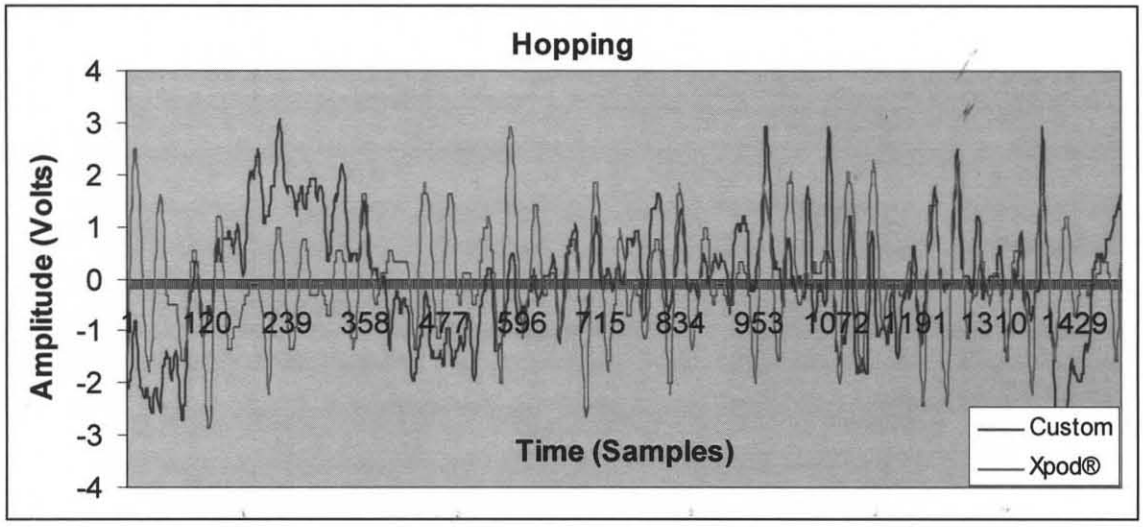

Figure 3.9 Raw PPG output from custom and Xpod®: Hopping activity.

The PPG signals during the hopping activity obtained from *both* sets of hardware were affected significantly by the high frequency motion artifact noise (Figure 3.9).

These PPG signals were quantified for motion artifact using signal to noise ratio (SNR) and Pearson correlation coefficient (R) measurements. These measurements were selected to compare the signal quality of the output of the custom and the Xpod® hardware. The SNR and R measured from the output signals are shown in Tables 3.5.

The signal to noise ratio was calculated by taking the ratio of the amplitude of the PPG signal and the amplitude of the noise. This measurement was performed by visually inspecting the amplitudes of signal and noise. A higher value of SNR signifies less noise and vice versa. The Pearson correlation coefficient (R) was calculated using LabVIEW® 8.0 based Pearson Correlation Coefficient.vi. A whole set of 60 seconds was used to calculate the R value. This coefficient represents the degree of association between two inputs The value of R always falls between -1 and 1; 0 signifies no correlation between the inputs (two inputs), +1 signifies that both the inputs are highly correlated, in fact, they are the same and -1 signifies that both inputs are associated inversely.

Table 3.5 Signal to Noise Ratio and Linear Coefficient (R) During Different Activities

Tasks	$SNR_{Xpod®}$	SNR_{Custom}	R
Sitting	0.94	0.88	0.779
Up/Down	0.91	0.4	0.336
Left/Right	0.83	0.5	0.203
Talking	0.9	0.7	0.5
Walking	0.85	0.6	0.45
Hopping	0.3	0.1	0.4

The Pearson's linear coefficient (R) was used an initial estimate of the PPG signal quality. As seen from Tables 3.5 and Figure 3.10, the linear correlation coefficient (R), obtained from the PPG signals (custom and Xpod® hardware PPG), was the maximum for the standard case – sitting - corresponding to no movement data and for other cases

that involved movement it reduced. Each of the R values shows a positive association i.e., no phase difference between the PPG signals (from Xpod® and custom hardware).

However, the results proved that this method should not be used as the only measure of signal quality because if the outputs from the Xpod® and the custom hardware (PPG signals) demonstrate similar noise profiles due to similar motion artifact, then the R would be a high value. In such cases, R values could lead to misleading conclusions. For example, a correlation value as high as 0.4 for the hopping activity case was seen. Figure 3.9 shows that the PPG signals from both the custom and the Xpod® hardware were affected significantly by the motion artifact noise. As the noise profiles of the PPG signals (from custom and Xpod®) were the same, the R value ended up being 0.4. In addition, a lower correlation value might not imply that the custom PPG is incorrect but that custom PPG is influenced more by motion artifact noise than the Xpod® PPG. Thus, proving that Xpod® includes a better motion artifact reduction algorithm. SNR of the signals was measured as a more thorough method of comparing the signal quality (Table 3.5).

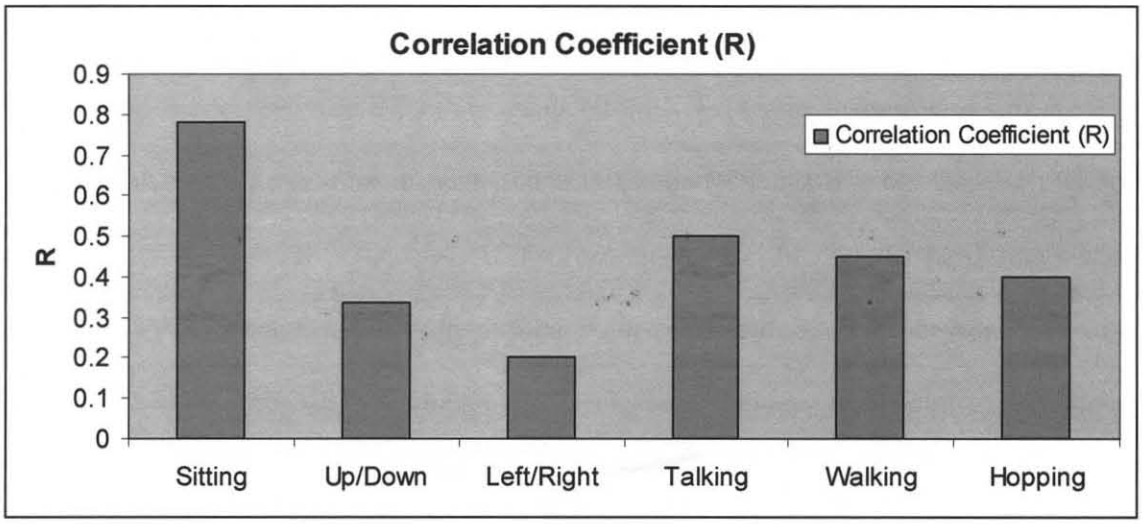

Figure 3.10 Correlation Coefficient plot for all the activities.

In the plots (Figure 3.11), the SNR calculated per activity is plotted for both the sets of hardware. The results in Figure 3.11 show that the SNR *decreased* during the activities as compared to the no activity case.

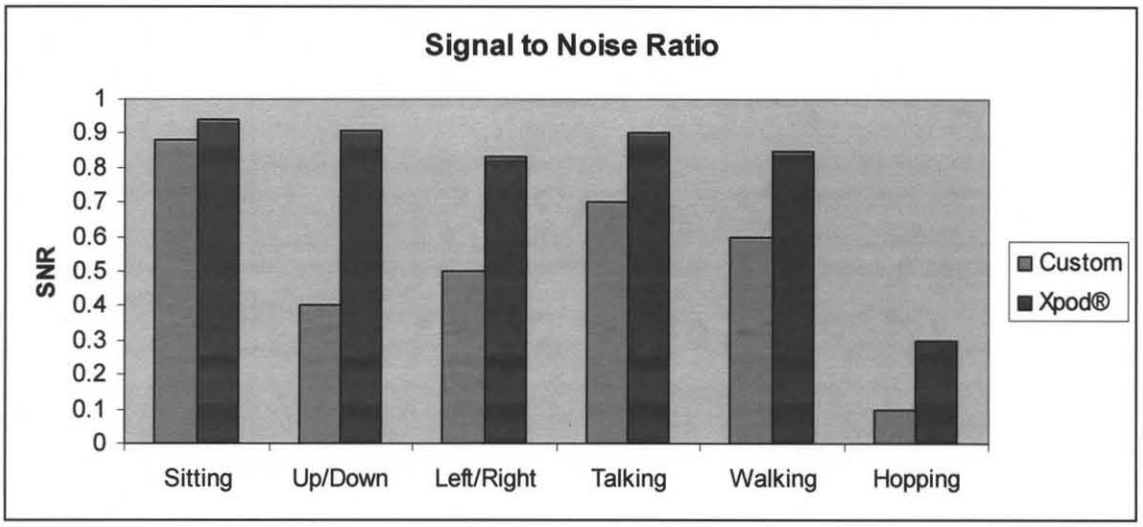

Figure 3.11 SNR of the PPG signal obtained from both the hardware during different activities.

Figures 3.4, 3.5 and 3.6 show the PPG output for the standard and head movement cases from both the hardware. The % SNR reduction was more for the custom PPG case than the Xpod® case for each activity, which implied that motion artifact were more pronounced in custom PPG case. The talking and walking activities did not affect the SNR of the custom PPG signal as much as the head movements did.

The hopping activity as seen in Figure 3.11 reduced the SNR of the PPG signals obtained from both the hardware. This reduction in SNR was due to the presence of high frequency motion artifact noise. The performance of the Xpod® and the custom, during hopping activity was similar (Figure 3.11).

3.2.1.3 Comparing Quantization Levels. One of the problems with the Xpod® output (as described in Chapter 2) was that its quantization level changes with blood perfusion,

i.e., for low blood perfusion, the output resolution deteriorates. From Figure 3.12, it is clear that the custom hardware provided a better quantization resolution than the Xpod®.

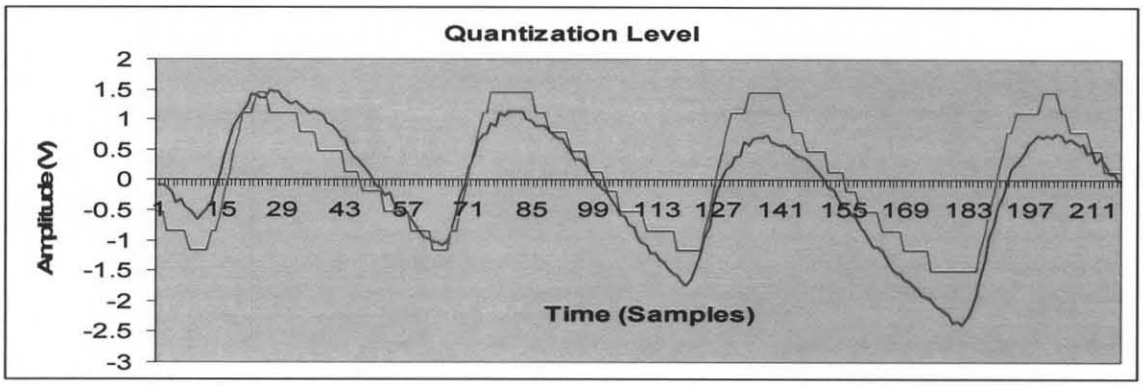

Figure 3.12 Verifying quantization resolution.

3.2.2 Software Verification Results

The breathing rate detection algorithm was explained in detail in Chapter 2. This section presents the impulse response of the digital elliptic IIR filter, which is the first stage of the detection algorithm. In addition, this section deals with verifying the efficiency of detection algorithm by comparing the output of the algorithm using the PPG signal from the custom and the Xpod® hardware, during paced breathing.

3.2.2.1 Digital Elliptic Filter Verification. A band pass elliptic filter with a low cutoff = 0.075 Hz, a high cutoff = 0.45 Hz, passband ripple = 0.1 dB, stopband ripple = 80 dB and order = 12 was applied to the stored PPG signal. The impulse response of the filter is provided in the figure below. The plot shows that the bandwidth of the filtered signal is restricted to approximately 4.5 – 27 breaths/minute.

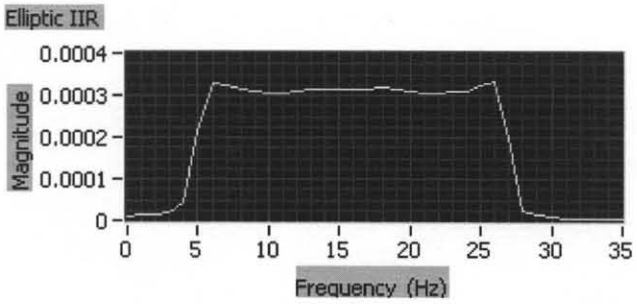

Figure 3.13 Impulse response of LabVIEW®-based digital elliptic filter.

3.2.2.2 Breathing Rate Detection Algorithm Verification using Known Input.

In order to test the accuracy of the detection algorithm, a known signal (sine waves with varying but known frequencies of 6, 9, 12 and15 Hz were used as an input. The program was tested for each of these frequencies as input. Results for 6 and 12 Hz are provided in the following section. 6 Hz was selected as one of the test frequencies to verify the algorithm's efficiency at low frequencies. 12 Hz sine wave input was also selected as it is the average normal breathing rate in adults.

The outcome of the detection algorithm is provided in the plots below for input frequencies of 6 and 12 Hz (Figures 3.14 – 3.16). The respiratory rate algorithm, as mentioned in Chapter 2, was based on the frequency with maximum magnitude in the power spectral density (PSD) waveform. Figure 3.14 shows the 6 Hz (left) and 12 Hz (right) sine wave inputs.

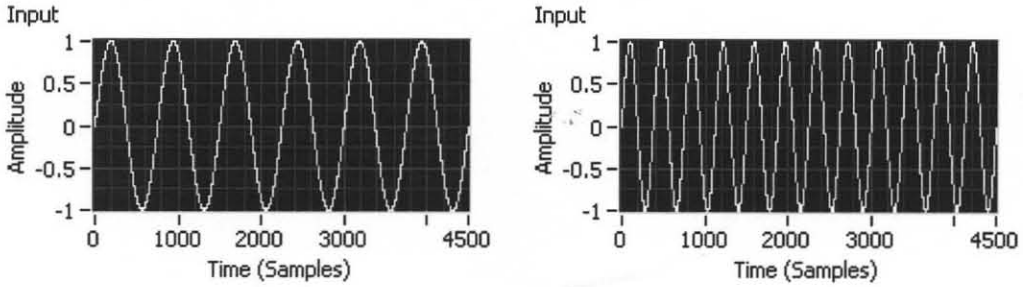

Figure 3.14 6 Hz (left) and 12 Hz (right) sine wave input to verify breathing rate detection algorithm.

Figure 3.15 shows the PSD waveform output. PSD waveform for 6 and12 Hz case shows a peak at the respective input frequencies. As mentioned in Chapter 2, a limit of 5 – 17 breaths per minute was applied to the frequencies (poles) detected using auto regressive (AR) coefficients. The frequencies in this range were separated as the respiratory rate candidates. The frequency with the maximum magnitude in the PSD was chosen from the candidates as the estimated breathing rate value. From the figure below (Figure 3.15), frequencies at 6 and 12 Hz have maximum magnitude, and thus were detected as the estimated breathing rate value as shown in Figure 3.16.

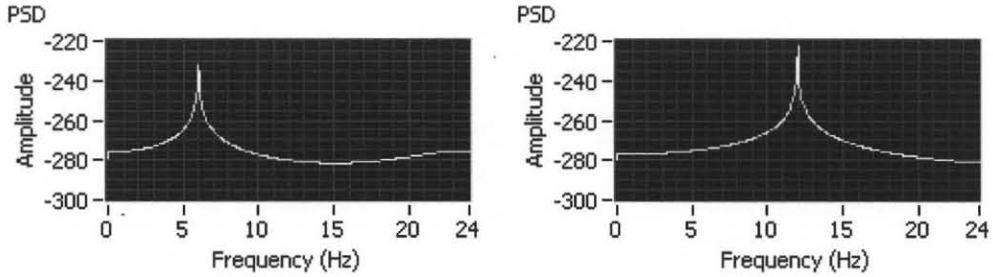

Figure 3.15 Power Spectral Density (PSD) response for 6 (left) and 12 (right) Hz sine wave input.

Figure 3.16 shows screen shots of the estimated breathing rate values after applying the algorithm.

Figure 3.16 Estimated respiration rate – output of breathing rate detection algorithm.

3.2.2.3 Breathing Rate Detection Algorithm (Paced breathing). After verifying the results for the known sine wave input, the PPG signals collected from N=1 individual during paced breathing (6, 9, 12 and 15 breaths per minute – 3 times in a

random order) were used as input to the detection algorithm. The results are as shown in the Tables 3.6 and 3.7 below:

Table 3.6 Results of Breathing Rate Detection Algorithm; Input: PPG from Custom Hardware – Output = (Estimated Breathing Rate)$_{Custom}$

***Custom* (Breaths per minute)**					
First Round		**Second Round**		**Third Round**	
True Value	Output	True Value	Output	True Value	Output
6	6.1	12	12.1	9	9.1
9	9.0	9	9.0	15	15.0
12	11.9	15	15.0	12	11.9
15	14.9	6	6.1	6	**11.9**

Table 3.7 Results of Breathing Rate Detection Algorithm; Input: PPG from Xpod® Hardware – Output = (Estimated Breathing Rate)$_{Xpod®}$

Xpod® (Breaths per minute)					
First Round		**Second Round**		**Third Round**	
True Value	Output	True Value	Output	True Value	Output
6	6.1	12	12.0	9	9.1
9	9.0	9	9.0	15	15.0
12	11.9	15	15.1	12	11.9
15	14.9	6	6.0	6	6.1

To explore the AR methods in more detail, the results (screen shots) of the breathing rate detection algorithm for the first round are presented. The respiratory induced intensity variations (RIIV) signal obtained by filtering the digitized PPG signal for each 6, 9, 12 and 15 breaths per minute case from both sets of hardware for the first round are presented in Figures 3.17 – 3.20. The plots on the right were obtained using PPG signals from the custom hardware and the ones on the left from the Xpod® hardware.

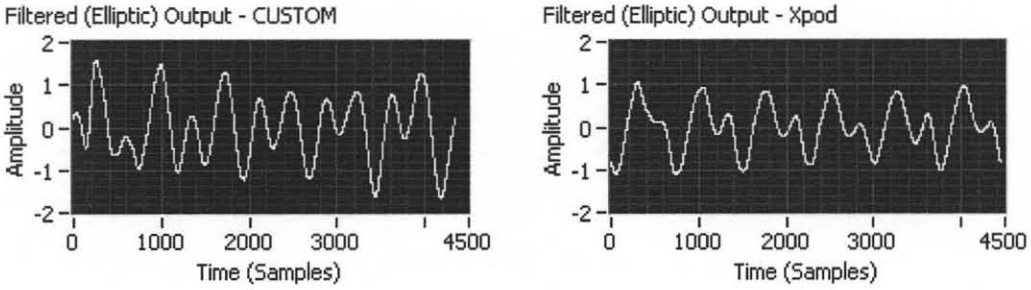

Figure 3.17 RIIV signal obtained by filtering the PPG signal from the Xpod® and the custom hardware using digital elliptic filter for 6 breaths per minute case.

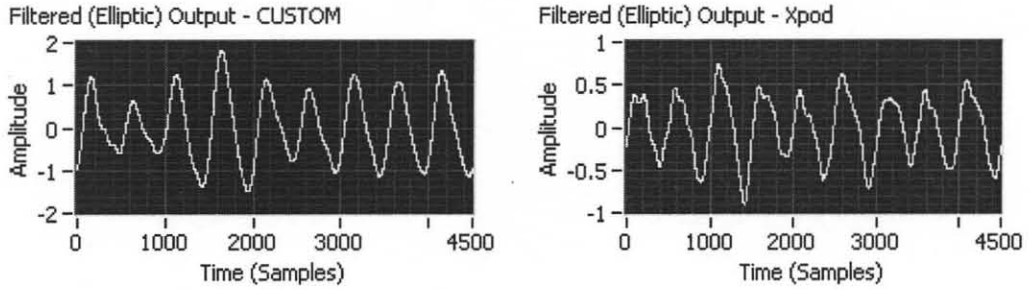

Figure 3.18 RIIV signal obtained by filtering the PPG signal from the Xpod® and the custom hardware using digital elliptic filter for 9 breaths per minute case.

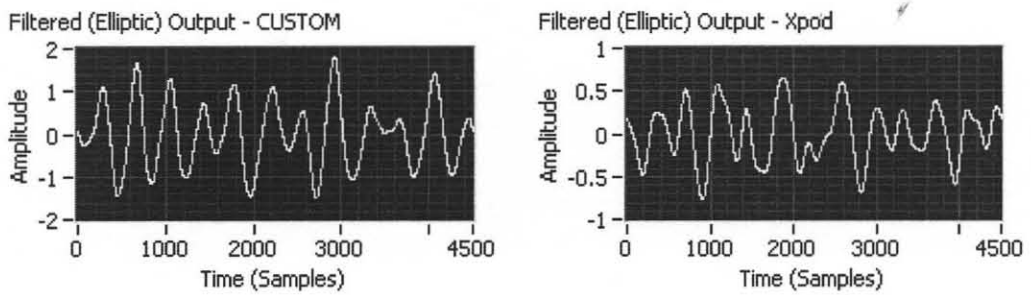

Figure 3.19 RIIV signal obtained by filtering the PPG signal from the Xpod® and the custom hardware using digital elliptic filter for 12 breaths per minute case.

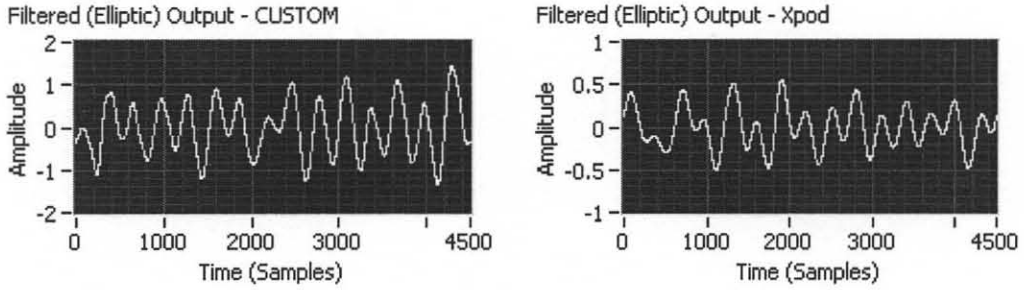

Figure 3.20 RIIV signal obtained by filtering the PPG signal from the Xpod® and the custom hardware using digital elliptic filter for 15 breaths per minute case.

Figures 3.21 – 3.24 shows the PSD waveform obtained from the down-sampled (1 Hz) and filtered PPG signal using AR modeling technique. There are several peaks in the 5-17 breaths per minute respiratory rate candidate group (explained in Chapter 2). However, the one with maximum magnitude was chosen as the estimated breathing rate and displayed. Figure 3.25 shows the output – estimated breathing rate - of the detection algorithm.

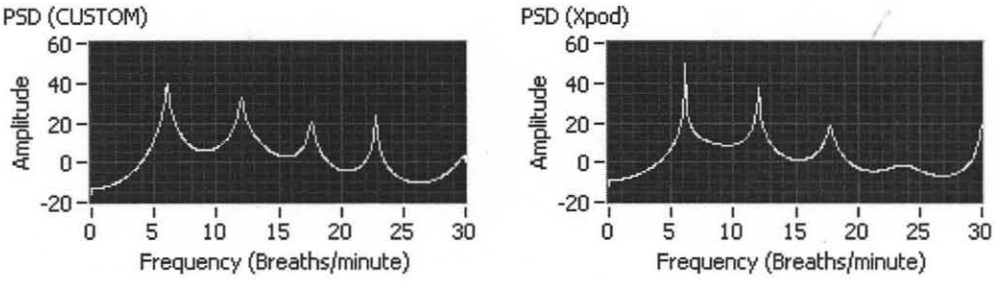

Figure 3.21 PSD of the filtered and downsampled PPG signal from the Xpod® (right) and the custom (left) hardware for 6 breaths per minute case.

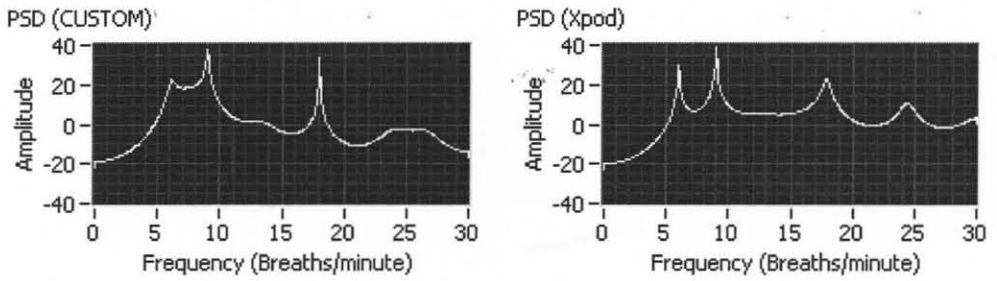

Figure 3.22 PSD of the filtered and downsampled PPG signal from the Xpod® (right) and the custom (left) hardware for 9 breaths per minute case.

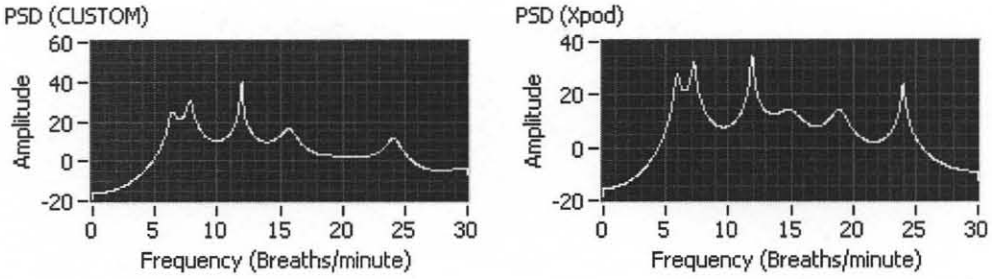

Figure 3.23 PSD of the filtered and downsampled PPG signal from the Xpod® (right) and the custom (left) hardware for 12 breaths per minute case.

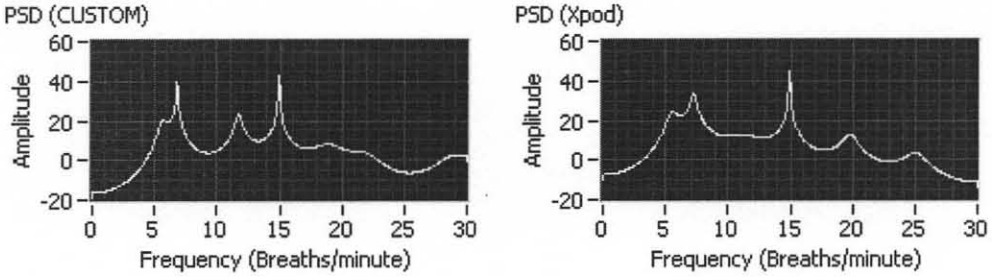

Figure 3.24 PSD of the filtered and downsampled PPG signal from the Xpod® (right) and the custom (left) hardware for 15 breaths/minute.

The screen shots of the estimated respiratory rates output, as shown in Figure 3.25, were recorded for all the paced breathing rates.

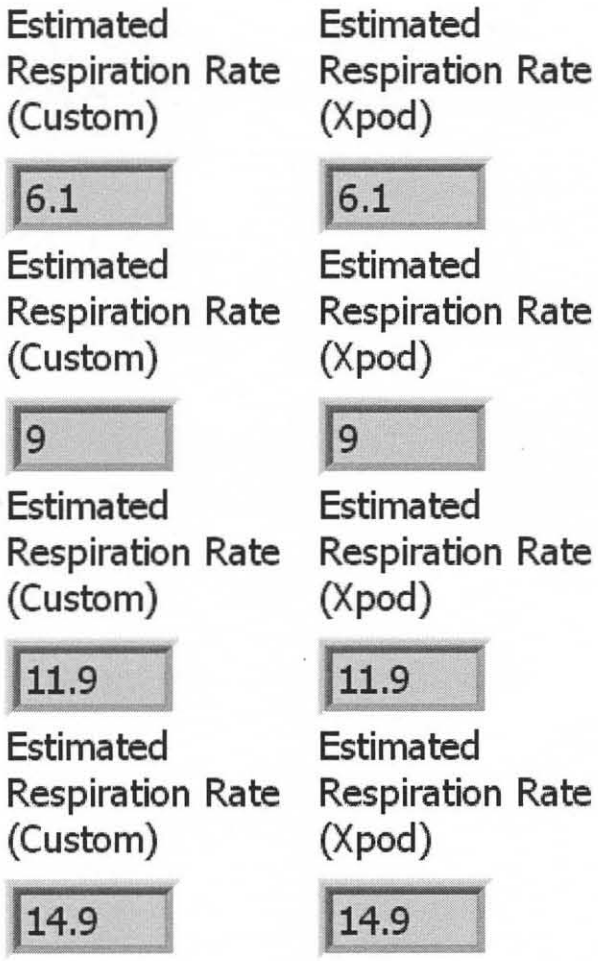

Figure 3.25 Estimated respiration rate – output of breathing rate detection algorithm for custom (left) and Xpod® (right) PPG (From top: 6, 9, 12, 15 breaths per minute input).

Table 3.8 Difference Between Estimated Breathing Rates (Custom – Xpod) Per Round

True Value	First Round	Second Round	Third Round
6	0	0.1	5.8
9	0	0	0
12	0	0.1	0
15	0	-0.1	0

As seen in Tables 3.6 and 3.7, the detection algorithm was applied to the PPG data obtained from one individual from the two sets of hardware during paced breathing. Difference between the estimated respiratory rates obtained using the two sets of PPG

signals (Custom - Xpod®) during paced breathing, was calculated per round. The results in Table 3.8 show that for 9, 12 and 15 breaths per minute case, a nominal difference of 0.1 breaths per minute was seen. The zeroes in this table signify that the estimated respiratory rates from the two sets of hardware were the same. The algorithm showed a discrepancy for 6 breaths per minute case with custom PPG signal as input during the third round. The plots for this case are presented in Section 3.2.2.3.

The repeatability graph as shown in Figure 3.26 was obtained by plotting (Estimated Breathing Rate) $_{\text{Xpod®}}$ on the X-axis and (Estimated Breathing Rate) $_{\text{Custom}}$ on the Y-axis per breathing rate per round. Clusters (3 values per breathing rate) of estimated breathing rates can clearly be seen for 9, 12 and 15 breaths per minute cases. For the 6 breaths per minute case, one outlier (as marked in Figure 3.26) was obtained. The possible reasons for its occurrence are discussed in Chapter 4.

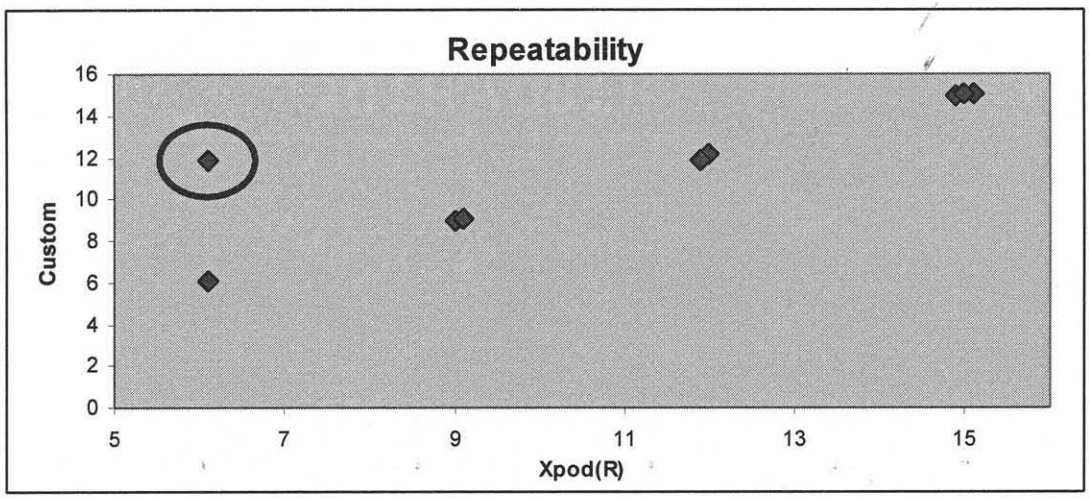

Figure 3.26 Repeatability graph for 6, 9, 12 and 15 breaths per minute case.

3.2.2.4 Erroneous Results from the Breathing Rate Detection Algorithm. From the original results presented in Table 3.6 and 3.7, it can be seen that there was a discrepancy in detecting the lowest paced breathing rate (6 breaths per minute), where

custom hardware PPG signal input provided erroneous rates only during the third round. Raw waveforms and algorithm results for both are shown below.

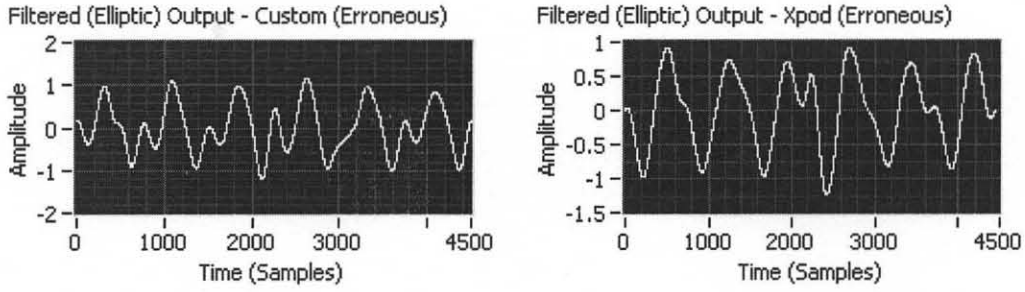

Figure 3.27 RIIV signal obtained by filtering the PPG signal from the custom hardware and the Xpod® for 6 breaths per minute case; Double peaks for each breath are detected

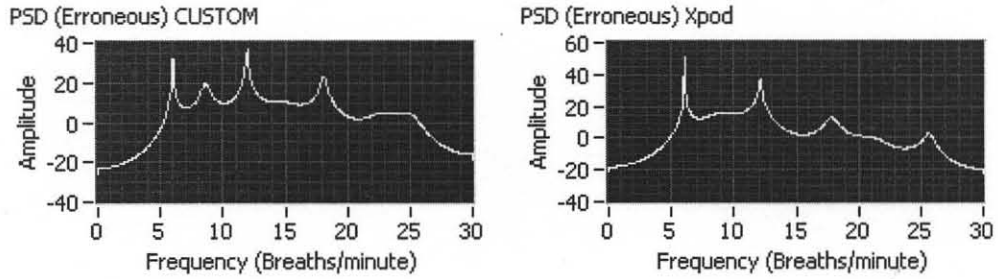

Figure 3.28 PSD of the filtered and downsampled PPG signal from the custom hardware and the Xpod®; Input PPG obtained during 6 breaths per minute paced breathing

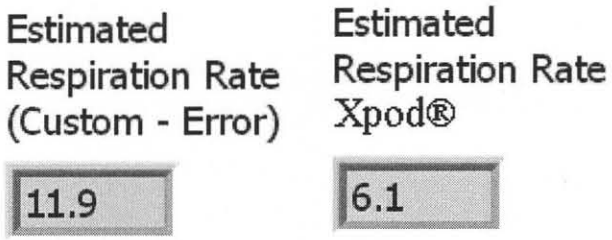

Figure 3.29 Estimated respiration rate – output of breathing rate detection algorithm (custom and Xpod® hardware – Erroneous 6 breaths/minute).

The possible reasons for these discrepancies are mentioned in further detail in Chapter 4.

CHAPTER 4

DISCUSSION

4.1 Hardware Verification

The frequency responses of the hardware-based high, low and notch filters reveal that the filters are able to filter out the unwanted frequencies quite efficiently in 0.1 – 5 Hz range. A control over the sampling rate, filtering characteristics, and quantization resolution is acquired pertaining to the custom design of the PPG hardware. This enables the flexibility of the system as compared to the off-the-shelf Xpod® module.

As mentioned in Chapter 1, the Xpod® module outputs PPG data in a serial format, which did not match the BlueSentry™ Bluetooth® module input requirement (analog in; 0 – 5 V only; no negative voltages). The output of the PPG custom hardware being analog can be adjusted to cast to the Bluetooth® module analog input requirements (0 - 5 V). This will enable reducing the number of transmitters per ambulatory pack and facilitate eight instead of four (with the current system) per computer (receiving station).

From the results shown in Chapter 3, it can be seen that the PPG signal obtained from the custom hardware was more significantly affected by the motion artifact due to the head and body movements as compared to the output of the Xpod® system. This is likely due to two main sources: 1) the design of the ear sensor, and 2) the ambient light incident on the photo diode 3) High pass filter cutoff. Due to propriety issues, it is difficult to find out if the Xpod® system has already considered these issues in their hardware design. To address these issues in the custom hardware design, the ear sensor design can be improved using a light-weight plastic clip and a spring with sufficient tension specifically designed for this application. In addition, a better mounting technique

for the LED and the photodiode can enhance the sensor's performance. The changes due to the ambient light can be reduced by adding a zeroing circuit, which subtracts out the artifact due to the unwanted light. The custom PPG signal can be made less prone to DC-drift or low frequency noise by adding AGC circuit to the hardware (Webster, 1997). Addressing these issues will help reduce some of the unwanted low frequency noise that can be falsely accounted as the RIIV signal.

The filters are designed to include respiratory rate derivation as a part of the PPG signal analysis. As a consequence, low frequency noise due to motion artifact is included in the output PPG signal. The low frequency noise spectrum overlaps the respiration frequency spectrum and thus, it is difficult to avoid noise. Changing the high pass filter cut off frequency value (0.1 Hz) to a higher value will cause exclusion of lower breathing rates. However, the motion artifact noise will be reduced. The Xpod® module is speculated to have a higher (more than 0.1 Hz) high pass cutoff than the custom hardware. From the results in Chapter 3, Figures 3.27 – 3.29, the PPG obtained from Xpod® successfully detected the low paced breathing rate (6 breaths per minute), while the custom PPG data produced erroneous results. The double peaks were more pronounced for custom PPG as compared to the Xpod® PPG, proving the higher high pass cutoff assumption true.

A few authors have also suggested using a motion detector as a part of the PPG sensor hardware. This enables detecting the motion of the sensor with head and body movements. This detected motion can be cancelled out from the PPG signal to obtain a motion artifact free output. Adding this functionality will enable differentiating between

the induced low frequency motion artifacts and the respiration (RIIV) signal in the raw PPG signals.

The Xpod® system used in the current ambulatory system costs $725 per individual, which includes the cost of the ear sensor (Model 8000Q), the analog processing module (Xpod®), the Blueport™ Bluetooth® module, and the receiver Bluetooth® module. If the current Xpod® system is replaced by the custom hardware system, the costs can be reduced to $80 per individual. This cost includes the passive and active analog processing circuit components and ear sensor components. Thus, building a custom hardware reduces the cost related to extra Bluetooth® transmitters and receivers. In addition, a custom hardware will help to increase the number of individuals per site (from four with the current system to eight) as number of transmitters can be reduced to half per ambulatory pack, which in turn will help reduce travel costs (HEMI study always outside of New Jersey).

4.2 Software Verification

This study was designed to use one of the best suggested methods for extracting respiratory rate from the PPG signal was used for this study. Autoregressive Modeling techniques are better in many respects than the classic Fourier Frequency Transform techniques to obtain power spectrum. The detection algorithm showed consistent results for the PPG signal obtained from both the custom and Xpod® hardware for most of the normal breathing range. The PPG signals obtained during 9, 12 and 15 breaths per minute, which fall in the normal respiratory rate range, produced a small difference (Custom – Xpod®) of 0.1 breaths per minute.

Only the lowest breathing rate (6 breaths per minute) in the third round produced a difference of 5.8 breaths per minute because the custom PPG signal input produced erroneous results. This discrepancy can be explained by several reasons. From Figure 3.27, it can be seen that the RIIV signal (output of digital elliptic filter) has double peaks resulting from one breath. This phenomenon causes over detection (6 detected as 12 breaths per minute) of the rate by the algorithm. Nilsson et al. (2000) provided two possibilities as a cause of this phenomenon: 1) Detection of respiratory rate variation from both the arterial and venous sides of the circulation, where a phase difference indicates two breaths, and 2) Disturbances from lower frequency variations in the blood pressure due to the THM waves as mentioned in Chapter 1, reflecting from the baroreflex loop (Nilsson et al., 2000). Therefore, lower respiratory rates increased the occurrence of false-positive breaths.

Another interesting phenomenon that can explain over detection is provided by Johansson et al. (1999). As discussed in Chapter 1, the RIIV signal arises from the changes in the venous return, which ultimately affects the peripheral venous pressure via peripheral blood volume change, due to the inspiration and expiration processes. According to Johansson et al. (1999), since thorax and abdomen plays an important role in the breathing process, the RIIV signal amplitude varies depending on the thorax and abdominal respiratory movements independently. A higher degree of thoracic respiration and higher respiratory rate gave rise to greater RIIV amplitudes. In addition, variations in posture and effects of body movements are assumed to affect the RIIV signal (Johansson et al., 1999). This phenomenon induces unpredictable changes in the amplitude of the

detected PPG signal at the periphery and might explain erroneous detection of the breathing rate (Figures 3.27 – 3.29, Chapter 3).

4.3 Future Goals

In order to verify the detection algorithm results more efficiently, a more controlled study using a pneumotachometer as a gold standard measurement of respiratory rate is suggested. Using a gold standard will further validate the output of the respiratory rate detection algorithm by eliminating the individual's compliance issues related to the paced breathing method.

CHAPTER 5

CONCLUSION AND FUTURE DEVELOPMENT

The main objectives of this thesis were: 1) to design LabVIEW based respiratory rate extraction algorithm from the PPG signals, 2) to build an analog PPG processing circuit and ear clip sensor to enhance the throughput of the current ambulatory setup being used for the HEMI study.

Several of the project goals were met, and other opportunities for improvement and future enhancements have been identified.

The respiratory rate extraction algorithm designed in LabVIEW can successfully extract respiratory rates from the PPG signal, although the effectiveness of the algorithm depends on the quality of the input PPG signal. A PPG signal contaminated with motion artifact noise will reduce the reliability of the algorithm. Thus, an input of artifact free PPG signal is one of the primary goals for a consistent performance of the algorithm. In addition, the PPG signal is sensitive to thoracic and abdomen respiratory movements and posture, which induces variations in the RIIV signal. A controlled study is suggested to account for the organ dependent variations in the RIIV signal. Understanding these variations, with a signal processing perspective, will help design more thorough extraction algorithm.

Building the custom PPG hardware does, in fact, increase the flexibility by enabling control over the sampling rate, filtering characteristics, quantization level etc. as compared to the off-the-shelf Xpod® module. The cost of the custom PPG hardware is significantly less as compared to the current Xpod® module. However, before

incorporating the custom PPG hardware in the current ambulatory setup a few obstacles have to be overcome.

The performance tests of the custom PPG signal compared to the Xpod® PPG signal revealed that motion artifact noise was more pronounced in the custom PPG signal. To resolve this issue, stringent filter cutoffs need to be applied to reduce the THM wave interference and the low frequency artifact noise, while still including the normal respiratory frequencies. In addition, a better ear clip sensor design will significantly reduce the motion artifact.

Due to apparently stringent filter cutoffs and better motion artifact handling capability, Xpod® PPG signal is hypothesized to estimate respiratory rates more reliably using the detection algorithm.

The future development for this project is to implement the changes suggested in this thesis:

- Stringent filter cutoffs in the hardware design
- Better ear sensor design
- Designing a motion reduction algorithm for the custom PPG signals apart from the filters
- Use a gold standard such as pneumotachometer to compare the respiratory rate detection algorithm

Heart rate and oxygen saturation measurements can also be extracted from the same raw data streams and be incorporated into the overall measurement system at a later stage.

APPENDIX A

OVERALL CIRCUIT

Figure A.1 shows the overall circuit of custom PPG hardware built for this study.

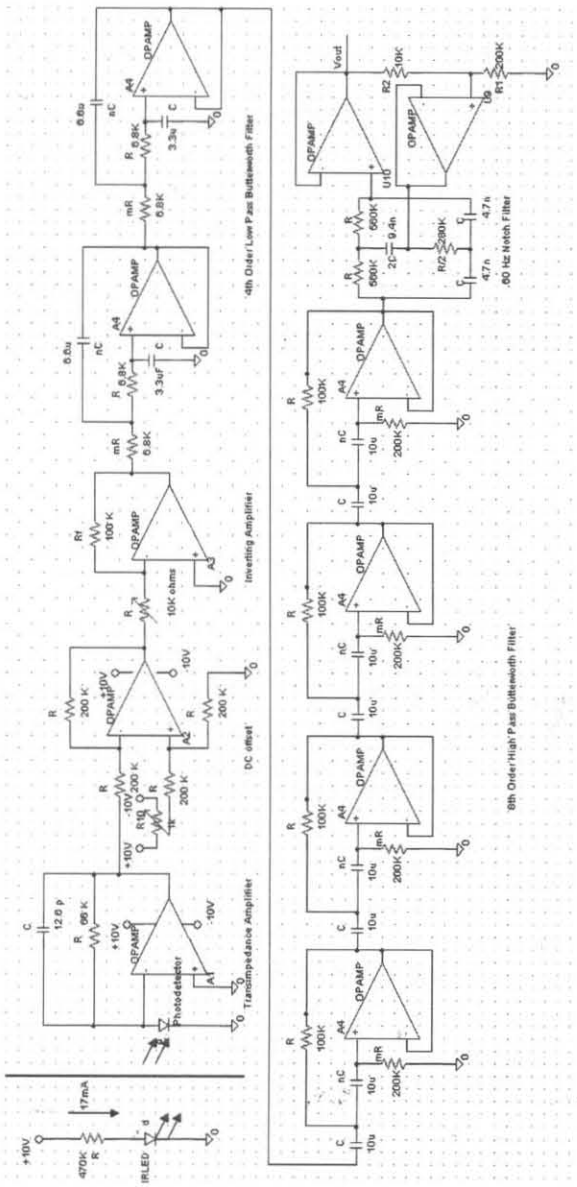

Figure A.1 Wiring diagram of the overall custom PPG hardware circuit.

APPENDIX B

DATA ACQUISITION PROGRAM

Figure B.1 shows the front panel of the data acquisition program built in LabVIEW 8.0.

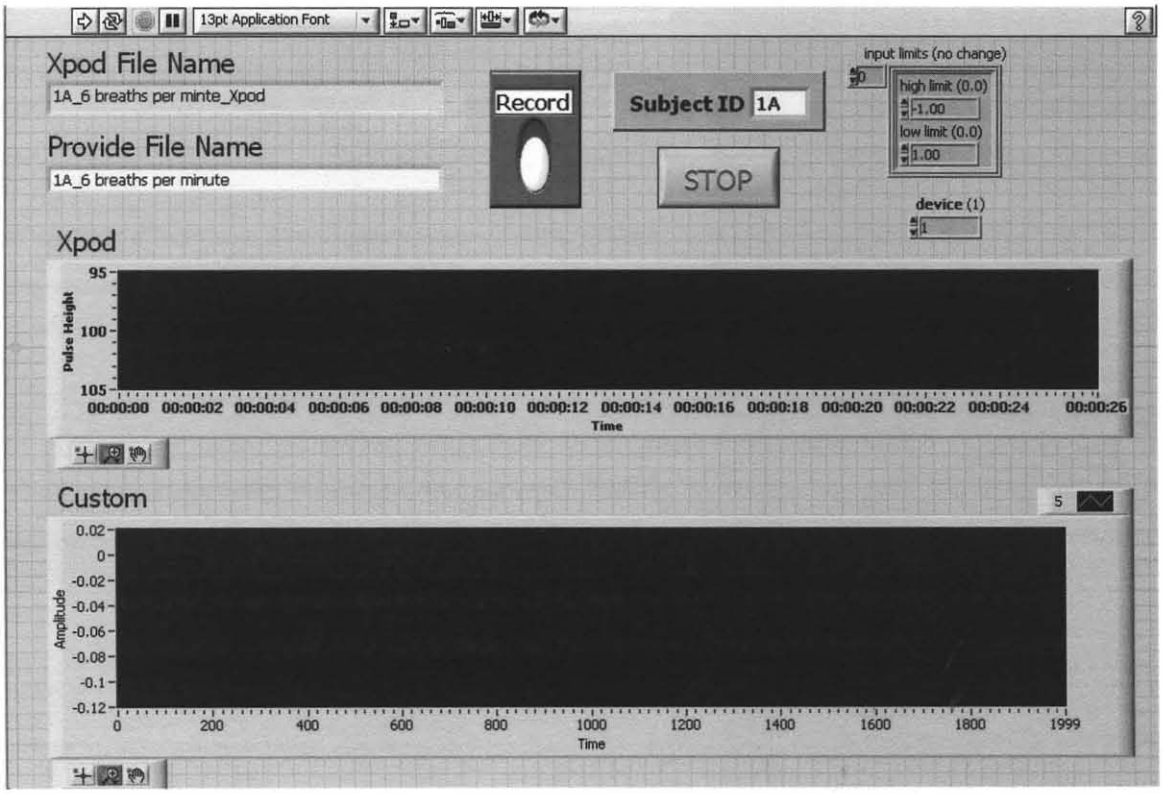

Figure B.1 Front panel of data acquisition program

APPENDIX C

CONTROLLED RESPIRATION

Figure C.1 shows the front panel of the paced breathing LabVIEW program.

Figure C.1 Front Panel of the paced breathing program: 12 breaths/min.

Figure C.2 shows the block diagram of the paced breathing LabVIEW program.

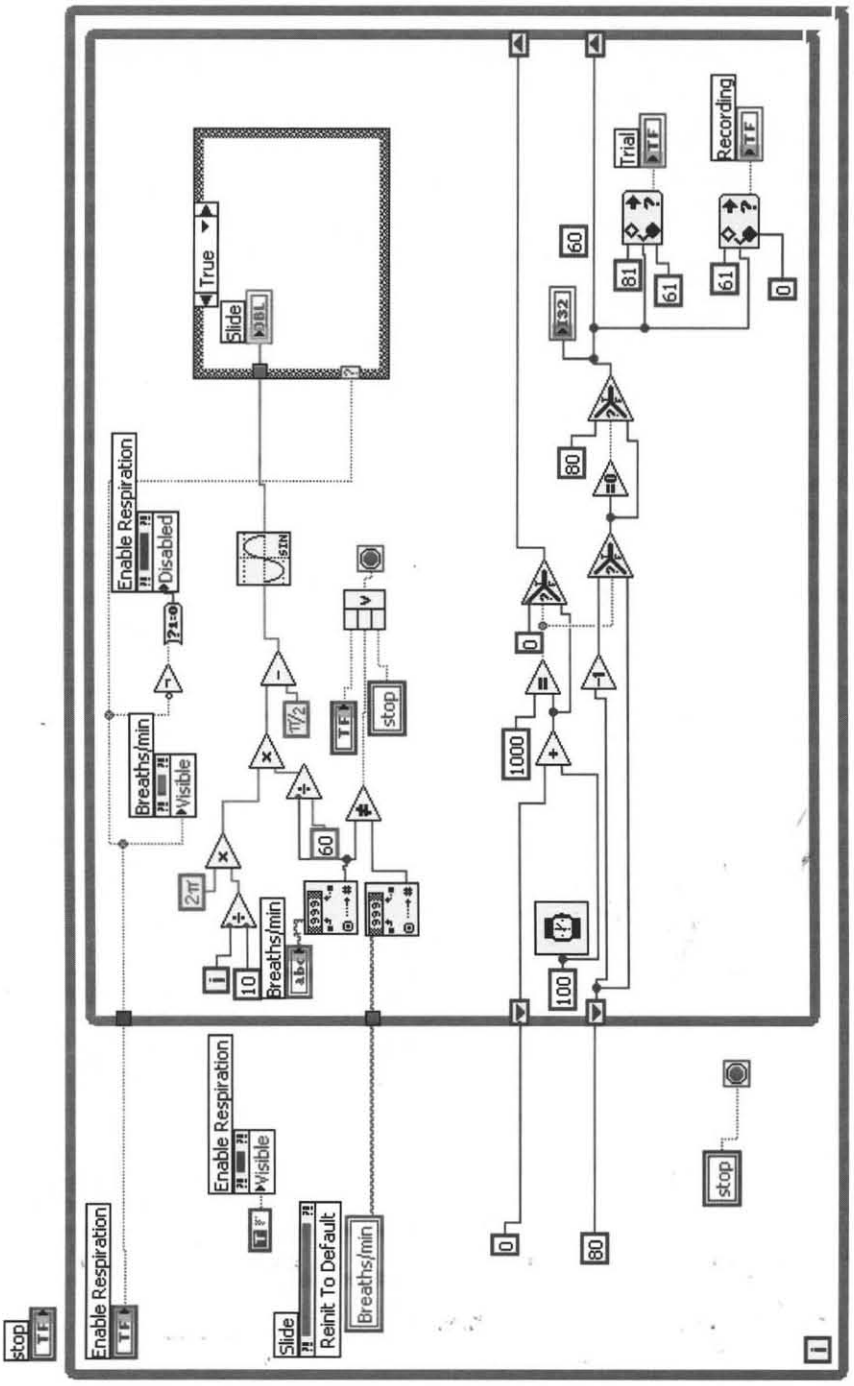

Figure C.2 Wiring diagram of the paced breathing program.

APPENDIX D

BREATHING RATE DETECTION ALGORITHM

Figure D.1 shows the first part (Sections 1, 2, and 3) of breathing rate detection program's block diagram in LabVIEW.

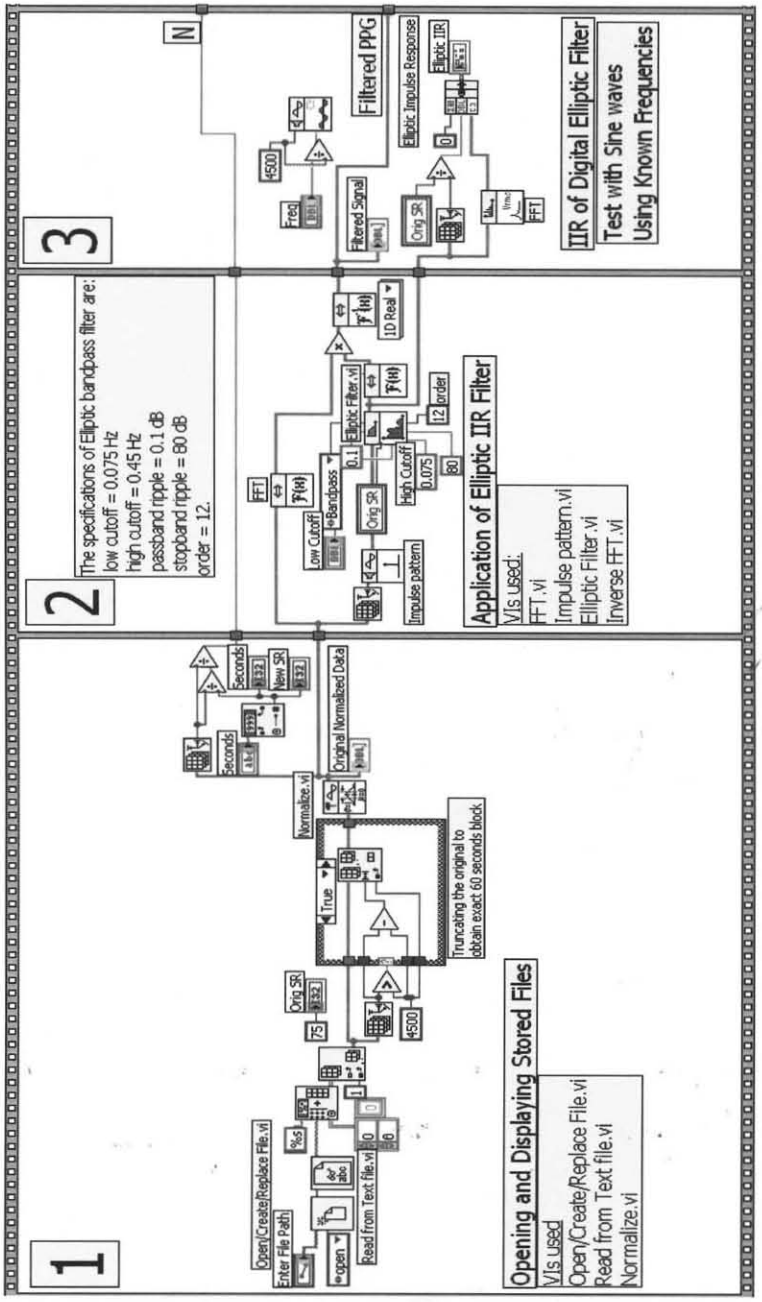

Figure D.1 Wiring diagram of the breathing rate detection program (Sections 1, 2 and 3).

Figure D.2 shows the second part (Section 4 – 4A, 4B and 4C) of breathing rate detection algorithm in LabVIEW.

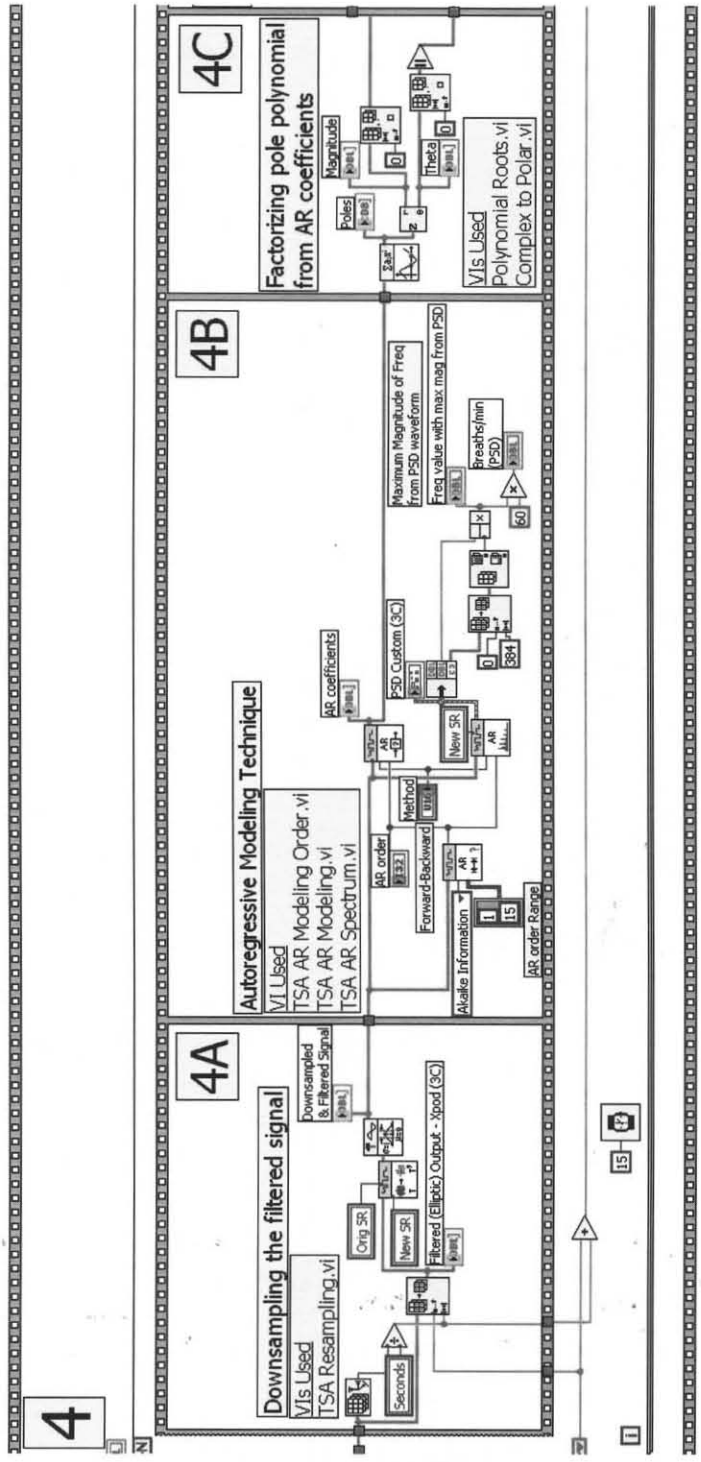

Figure D.2 Wiring diagram of the breathing rate detection program (Sections 4 – 4A, 4B and 4C).

Figure D.3 shows the last part (Section 4 – 4D, 4E, 4F and Final Output) of breathing rate detection algorithm in LabVIEW.

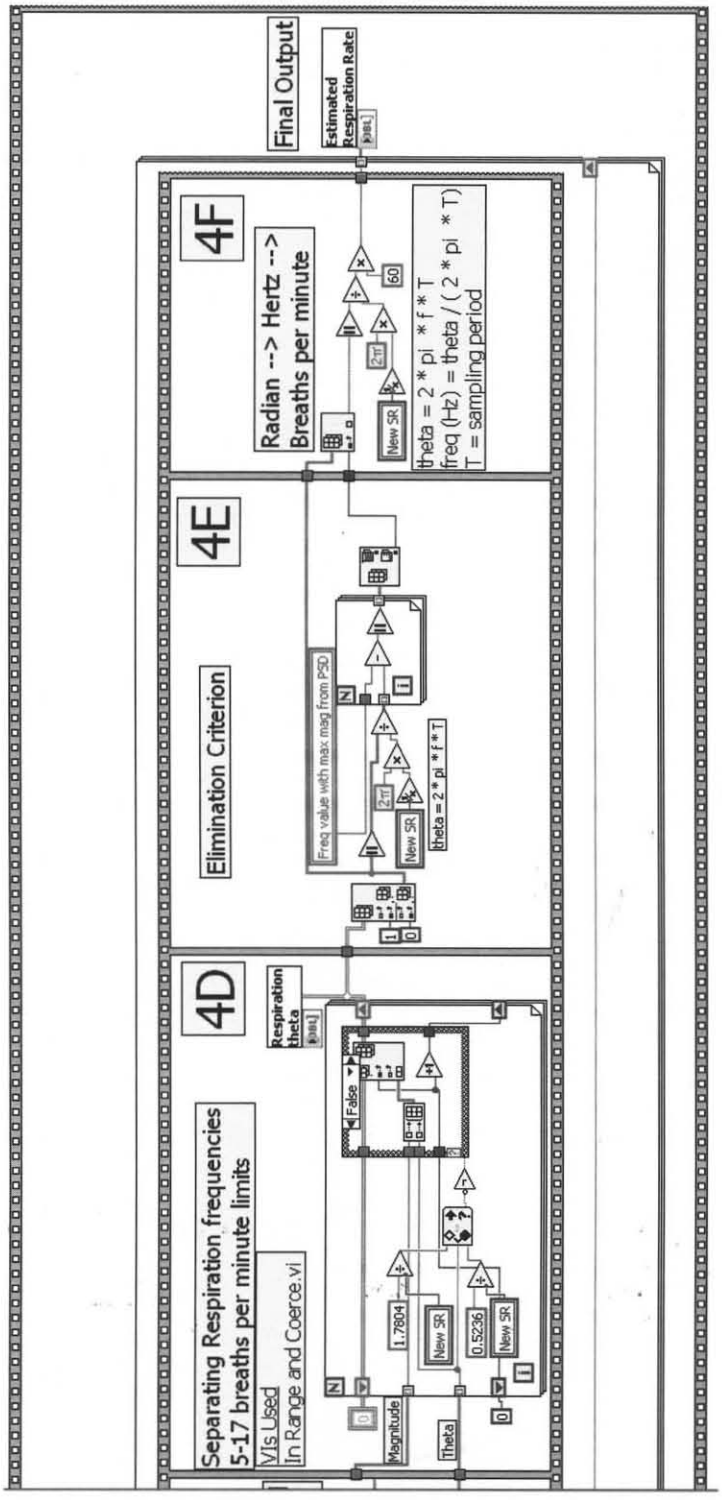

Figure D.3 Wiring diagram of the breathing rate detection program (Sections 4 – 4D, 4E, 4F and Final Output).

REFERENCES

Anon. (2001–07). Circulatory System in *The Columbia Encyclopedia, 6th ed.* New York: Columbia University Press. Retrieved January 20, 2008 from www.bartleby.com/65/.

Anon. Human Cardiovascular System. Online Art in Encyclopædia Britannica Online. Retrieved 17 Jan. 2008 from Website: http://www.britannica.com/eb/article-33573/human-cardiovascular-system.

Anon. respiration, human. Online Art in Encyclopædia Britannica Online. Retrieved Jan. 13, 2008 from http://www.britannica.com/eb/art-99770.

Acharya, U.R., Suri, J.S., Spaan, J.A.E., Krishnan, S.M. (2007). *Advances in Cardiac Signal Processing.* New York: Springer.

Akay, Metin (1994). *Biomedical Signal Processing.* San Diego: Academic Press Inc.

Berne, Robert M., Levy, Matthew N. (2001). *Cardiovascular Physiology.* Philadelphia, PA: Mosby.

Beverley J. Hunt (2002). *An introduction to vascular biology [electronic resource]: from basic science to clinical practice.* New York: Cambridge University Press.

Brecher, G.A., Hubay, C.A. (1954). Pulmonary Blood Flow and Venous Return During Spontaneous Respiration. *Am. J. Physiol., 111*, 210.

Chang, David W. (2001). *Clinical Application of Mechanical Ventilation.* Thomson Delmar Learning, 207.

Fleming, S. G., Tarassenko, L. (2007). A Comparison of Signal Processing Techniques for the Extraction of Breathing Rate from the Photoplethysmogram. *PWASET, 24*, 276-280.

Franco, Sergio (1988). *Design with Operational Amplifiers and Analog Integrated Circuits.* New York: McGraw-Hill Inc.

Johansson, A., Oberg, P.A. (1999). Estimation of respiratory volumes from the photoplethsymographic signal. Part I: Experimental results. *Med. Biol. Comput., 37*, 42-47.

Johansson A., Stromberg, T. (2000). Influence of Tidal Volume and Thoraco-Abdominal Separation on the Respiratory Induced Variation of the Photoplethsmogram. *J Clinical Monit., 16*, 575-581.

K. Shelley and S. Shelley (2001). Pulse Oximeter Waveform: Photoelectric Plethysmography. *Clinical Monitoring*, 420-428.

Lane, N., Oxygen (2004). *The Molecule that Made the World.* Oxford University Press, USA.

Nakajima, K., Tamura T., Miike, H. (1996). Monitoring of heart and respiratory rates by photoplethysmography using a digital filtering technique. *Med. Eng. Phys., 18-5*, 365-372.

Nilsson, L., Johansson, A., Kalman, S. (2003). Respiratory variations in the reflection mode photoplethysmographic signal. Relationships to peripheral venous pressure. *Med. Biol. Eng. Comput., 41*, 249-254.

Nilsson L., Johansson, A., Kalman, S. (2000). Monitoring of Respiratory Rate in Postoperative Care Using a New Photoplethysmographic Technique. *J Clinical Monit., 16*, 309-315.

Photodiode Technical Guide. Retrieved February 23, 2008 from Hamamatsu Website: http://sales.hamamatsu.com/assets/html/ssd/si-photodiode/index.htm

Rusch, T. L., Sankar, R., Scharf, J. E. (1996). Signal Processing Methods for Pulse Oximetry. *Comput. Biol. Med.*, 26 – 2, 143-159.

Sleight, P. (1995). Physiology and Pathophysiology of Heart Rate and Blood Pressure Variability in Humans. Is Power Spectral Analysis Largely an Index of Baroreflex Gain? *Clinical Science, 88*, 103-109.

Stern, Robert M., Ray, William J., Quigley, Karen S. (2001). *Physiological Recording.* New York: Oxford University Press Inc.

Ubeyli, E., Cvetkovic, D., Cosic, I. (2007). AR Spectral Analysis Technique for Human PPG, ECG, and EEG Signals. *J Med. Syst.*

Webster, J.G. (1997). *Design of Pulse Oximeters.* New York: Taylor & Francis Group.